New mouse models for high resolution and live imaging of planar cell polarity proteins in vivo

Lena P. Basta[1], Michael Hill-Oliva[1,2], Sarah V. Paramore[1], Rishabh Sharan[1], Audrey Goh[1], Abhishek Biswas[1,3], Marvin Cortez[1], Katherine A. Little[1], Eszter Posfai[1] and Danelle Devenport[1,4]

[1] Department of Molecular Biology, Princeton University, Princeton, NJ 08544 USA

[2] Department of Medicine, Columbia University, New York, NY 10032 USA

[3] Research Computing, Office of Information Technology, Princeton University, Princeton, NJ 08544, USA.

[4]Correspondence to danelle@princeton.edu

Abstract

The collective polarization of cellular structures and behaviors across a tissue plane is a near universal feature of epithelia known as planar cell polarity (PCP). This property is controlled by the core PCP pathway, which is comprised of highly conserved membrane-associated protein complexes that localize asymmetrically at cell junctions. Here we introduce three new mouse models for investigating the localization and dynamics of transmembrane PCP proteins Celsr1, Fz6, and Vangl2. Using the skin epidermis as a model, we characterize and verify the expression, localization and function of endogenously-tagged Celsr1-3xGFP, Fz6-3xGFP and tdTomato-Vangl2 fusion proteins. Live imaging of Fz6-3xGFP in basal epidermal progenitors reveals that the polarity of the tissue is not fixed through time. Rather asymmetry dynamically shifts during cell rearrangements and divisions, while global, average polarity of the tissue is preserved. We show using super-resolution STED imaging that Fz6-3xGFP and tdTomato-Vangl2 can be resolved, enabling us to observe their complex localization along junctions. We further explore PCP fusion protein localization in the trachea and neural tube, and discover new patterns of PCP expression and localization throughout the mouse embryo.

© 2021. Published by The Company of Biologists Ltd.

Development • Accepted manuscript

Introduction

Planar cell polarity (PCP) describes the coordinated alignment of cell polarity across a tissue plane, and is exemplified by polarized protrusions that emanate from epithelial surfaces such as bristles, hairs, scales, and motile cilia (Apodaca, 2018; Devenport, 2016; Goodrich and Strutt, 2011; Iwasaki et al., 2018; Schweisguth, 2015; Wallingford and Mitchell, 2011). The PCP pathway, a highly conserved set of membrane associated proteins, orients these diverse structures and directs a range of polarized behaviors including cell rearrangements and oriented cell divisions (Butler and Wallingford, 2017; Carroll and Yu, 2012; Segalen and Bellaïche, 2009; Wallingford, 2012). Landmark studies in *Drosophila* identified the 'core' PCP components through mutations that cause cuticular bristles and wing hairs to form disordered patterns (Adler, 2012; Carvajal-Gonzalez and Mlodzik, 2014; Goodrich and Strutt, 2011; Maung and Jenny, 2011). The core PCP components were later shown to have multiple orthologs in vertebrates and new, vertebrate-specific PCP functions including convergent extension, ciliogenesis and neural tube closure (Adler and Wallingford, 2017; Butler and Wallingford, 2017; Jussila and Ciruna, 2017; Nikolopoulou et al., 2017; Sutherland et al., 2020; Wang et al., 2019). Importantly, human mutations in PCP genes are associated with neural tube defects, ciliopathies, and congenital heart defects linking the PCP pathway to structural birth defects in humans (Cai and Shi, 2014; De Marco et al., 2014; Wang et al., 2019). Given the expansion of PCP functions in vertebrates and the implications of PCP in human disease, it is important to define the features that are both conserved and unique to vertebrate PCP. A necessary step toward this goal is the development of tools to investigate the cell biology of core PCP components in vertebrate model systems.

The core PCP pathway is comprised of a set of transmembrane and cytoplasmic proteins that asymmetrically localize to cell junctions. On one side of the cell, transmembrane protein Frizzled (Fz), colocalizes with cytoplasmic protein Dishevelled (Dvl), while Vangl (Van Gogh, Vang, in *Drosophila*) and its cytoplasmic partner Prickle (Pk), localize to the opposite side. A third transmembrane protein, Celsr (Flamingo, Fmi, in *Drosophila*), localizes to both sides of the cell, forms homophilic adhesions, and helps to bridge opposing complexes of Fz-Dvl and Vangl-Pk across cell interfaces (Figure 1A) (Butler and Wallingford, 2017; Devenport, 2014; Harrison et al., 2020; Strutt and Strutt, 2009; Yang and Mlodzik, 2015). Whether all vertebrate tissues exhibit these asymmetries is still unclear, in part due to limitations of the tools used for visualizing PCP distributions (Jones and Chen, 2007; Wang and Nathans, 2007). Antibodies for

Development • Accepted manuscript

immunofluorescence vary in quality, and overexpression of PCP components often perturbs their localization and function. Further, PCP proteins must be expressed clonally or mosaically to determine whether their distribution is unipolar because conventional light microscopy cannot resolve the two sides of a junction (Olofsson and Axelrod, 2014). Recent advances in CRISPR-Cas9 technology, however, provide an efficient means to introduce fluorescent proteins into endogenous loci, helping to overcome the issues arising from transgenic overexpression (Gu et al., 2018). Moreover, super resolution microscopy can resolve asymmetries across junctional interfaces without the need for clones or mosaics (Ezan and Montcouquiol, 2013; Stahley et al., 2021; Wegel et al., 2016). These technological advances provide an opportunity to clarify ambiguities and conflicting reports regarding PCP protein localization in the vertebrate literature.

During polarization, PCP proteins redistribute from initially uniform distributions (Devenport, 2014). Live imaging studies in *Drosophila* were the first to monitor PCP protein dynamics over the course of polarization. These studies revealed directed transport of Fz and Dvl-containing membrane vesicles toward the proximal side of wing epithelial cells (Matis et al., 2014; Shimada et al., 2006). Using FRAP in the *Drosophila* wing, PCP proteins were shown to assemble into highly stable punctate assemblies at polarized junctions whereas non-punctate regions displayed higher mobility and turnover (Strutt et al., 2016; Strutt et al., 2011). Differential stability of PCP proteins along the axis of asymmetry has also been observed in *Xenopus* epidermis (Butler and Wallingford, 2015; Chien et al., 2015), neural plate (Butler and Wallingford, 2018), as well as the mouse oviduct (Shi et al., 2016), suggesting that the regulation of clustering and aggregation of PCP complexes is an important, conserved mechanism in establishing PCP. Studies of PCP protein dynamics in mouse are much more limited in part due to the difficulties associated with live imaging embryonic development in utero and due to a lack of mouse models suitable for visualizing PCP proteins in living tissue.

Following polarization, asymmetrically localized PCP proteins act on downstream, cytoskeletal factors to polarize epithelial protrusions like wing hairs, bristles, or cilia (Devenport, 2016). In vertebrates, PCP asymmetry also induces large scale convergent extension movements through cell intercalation driven by polarized cell crawling and junctional remodeling (Huebner and Wallingford, 2018; Shindo et al., 2018; Sutherland et al., 2020; Tada and Heisenberg, 2012). In the *Xenopus* neuroectoderm, for example, enrichment of PCP proteins at cell junctions correlates with actomyosin recruitment and junction shrinkage to drive convergent extension (Butler and Wallingford, 2018). The impact of cell rearrangements, where junctions must

Development • Accepted manuscript

dissolve and reform, on PCP asymmetry is unknown. Is asymmetry continually refined and reestablished during cell rearrangements? Furthermore, how is the long-range, coordinated asymmetry of PCP proteins preserved in highly proliferative tissues as cells round up, divide, and establish new junctions with their neighbors?

Here we use 2C-HR-CRISPR (Gu et al., 2018) to introduce fluorescent tags in the endogenous loci of the three core transmembrane PCP components, Celsr1, Fz6 and Vangl2. We show that Fz6-3xGFP, tdTomato-Vangl2, and Celsr1-3xGFP strains are viable and display bright PCP protein labeling from their endogenous loci. We use live imaging of the mouse epidermis to show how, despite extensive cell divisions and cell rearrangements throughout the tissue, the average planar polarity of epidermal progenitor cells is maintained through continuous, local repolarization events. We further show using super-resolution imaging how these tools allow us to resolve the asymmetric partitioning of Fz6-3xGFP and tdTomato-Vangl2 to opposite sides of cell junctions without the use of chimeras or mosaic expression. Finally, we discover new patterns of PCP gene expression and protein localization throughout the mouse embryo.

Results

Generating endogenously tagged Celsr1-3xGFP, Fz6-3xGFP and tdTomato-Vangl2 mouse lines

To generate mouse strains that express fluorescently-tagged PCP proteins from their endogenous loci, we used 2C-HR-CRISPR to insert 3xGFP at the intracellular, C-terminus of Celsr1 and Fz6 (Fig. 1B,D), and tdTomato at the N-terminus of Vangl2 (Fig. 1F) (Gu et al., 2020b). All three are multipass transmembrane proteins, but unlike Celsr1 and Fz6, Vangl2 is a four-pass transmembrane protein with cytosolic domains at both N- and C-termini. The N-terminus of Vangl2 was chosen for tagging to avoid interfering with a highly conserved, C-terminal PDZ-binding motif (Bailly et al., 2018; Kibar et al., 2001b; Murdoch et al., 2001; Park and Moon, 2002; Torban et al., 2004; Y. and Katoh, 2005). 3xGFP was inserted in frame and upstream of *Celsr1* and *Fz6* stop codons (Fig. 1C,E), and tdTomato in frame and downstream of the *Vangl2* start codon (Fig. 1G). Founder mice were screened for GFP or tdTomato insertion, outcrossed and sequenced to ensure correct and mutation-free targeting of the fluorescent tag. Celsr1-3xGFP and Fz6-3xGFP knock-in lines were homozygous viable and fertile, and did not

Development • Accepted manuscript

display any known PCP phenotypes. By contrast, although heterozygous tdTomato-Vangl2 mice were viable and fertile, homozygous animals at postnatal stages displayed curly tails, hermaphroditism, and head shaking behaviors. At embryonic stages, tdTomato-Vangl2 homozygotes presented variably and incompletely penetrant neural tube closure defects including curly tails, spina bifida, anencephaly or, most severely, craniorachischisis. These phenotypes were less severe than those caused by loss-of-function mutations in the Vangl2 gene (Kibar et al., 2001a; Kibar et al., 2001b; Murdoch et al., 2001; Torban et al., 2008), but nevertheless they indicate that fusion of tdTomato to the N-terminal cytoplasmic domain does impair some Vangl2 functions.

Celsr1-3xGFP, Fz6-3xGFP and tdTomato-Vangl2 show proper localization and function in the embryonic epidermis

To verify that Celsr1-3xGFP, Fz6-3xGFP, and tdTomato-Vangl2 fusion proteins were functional, we characterized their expression, localization and function in the skin epidermis where the PCP pathway directs the orientation of hairs across the skin surface. PCP proteins are expressed in basal cells of the interfollicular epidermis (IFE), the progenitors that give rise to hair follicles and the skin's outer stratified layers (Chang et al., 2016; Devenport and Fuchs, 2008). As early as embryonic day 11.5 (E11.5), PCP proteins become asymmetrically localized and over development, asymmetry increases in magnitude and alignment, peaking around E15.5 (Aw et al., 2016; Devenport and Fuchs, 2008). The polarized distribution of PCP proteins specifies the direction of hair follicles, which bud from polarized basal cells and point in an anterior orientation (Fig. 2). Hair follicle polarity is lost or randomized in PCP mutants, and PCP proteins become uniformly distributed within cells (Cetera et al., 2017; Chang et al., 2016; Devenport and Fuchs, 2008; Guo et al., 2004; Ravni et al., 2009; Wang et al., 2006b; Wang et al., 2010). If Celsr1-3xGFP, Fz6-3xGFP, and tdTomato-Vangl2 fusion proteins impair PCP function, we expect to observe reduced asymmetric localization and hair follicle misalignment.

In sagittal views of E16.5 epidermis, Celsr1-3xGFP Fz6-3xGFP, and tdTomato-Vangl2 fusion proteins were expressed in the basal layer of the IFE and developing hair follicles (Fig. 2A-C), similar to their previously reported expression in wild-type epidermis using immunofluorescence (Devenport and Fuchs, 2008). Nascent hair follicles emerged from the epithelium with an anterior-directed tilt, and displayed normal growth and morphology (Fig. 2A-C). To quantify hair follicle polarization, flat mounted E15.5 backskins were imaged and tiled to capture hundreds of

Development • Accepted manuscript

hair follicles across the skin surface and the angle of hair follicle growth was measured relative to the anterior-posterior axis. In all three lines, developing hair follicles pointed anteriorly and collectively aligned along the A-P axis, and their distributions were indistinguishable from wild-type epidermis (Fig. 2D-G, Supplemental Fig. 1). Notably, in homozygous tdTomato-Vangl2 embryos, hair follicles were properly aligned even in embryos with neural tube closure defects, indicating that although the fusion protein is partially impaired in the neural tube, it is largely functional in the skin (Supplemental Fig. 1D-E).

To characterize PCP protein localization and asymmetry in the epidermis, we compared the distributions of Celsr1-3xGFP, Fz6-3xGFP, and tdTomato-Vangl2 at E15.5 to the distribution of their corresponding untagged proteins in control embryos. We used automated segmentation (see *Methods*) to detect basal cell edges using E-Cadherin, and calculated the nematic order of Celsr1-3xGFP, Fz6-3xGFP and tdTomato-Vangl2 distributions. Compared to E-Cadherin, which was localized uniformly at basal cell edges, endogenously-tagged PCP proteins were enriched along anterior-posterior junctions (Fig. 3A-E). Importantly, their polarized distributions were similar in magnitude and collective alignment to their untagged counterparts in control embryos (Fig. 3F-H). Moreover, the distribution of other PCP components was unaffected in each of the endogenously-tagged mouse lines (Supplemental Fig. 2A-D). For example, Vangl2, whose asymmetric localization relies on Celsr1 (Devenport and Fuchs, 2008; Stahley et al., 2021), was correctly polarized in Celsr1-3xGFP epidermis (Supplemental Fig. 2A) and was comparable to Vangl2 localization in wild-type controls (Fig. 3H). Again, despite the variable neural tube defects in tdTomato-Vangl2 homozygous embryos, we did not observe a difference in tdTomato-Vangl2 distribution in the epidermis of embryos with open or closed neural tubes (Fig. 3C-D) and the distribution in both was comparable to the untagged protein in control embryos (Fig. 3H).

Overall, these data indicate that fusion of 3xGFP and tdTomato onto the transmembrane PCP components does not impair their expression, localization or function in the epidermis. Moreover, proper expression and localization of tdTomato-Vangl2 in the basal layer, along with the lack of hair follicle phenotypes, indicates although the tdTomato insertion interferes Vangl2 function in the neural tube, it does not appear to affect its function in the epidermis, even when homozygous.

Development • Accepted manuscript

Resolving Fz6-3xGFP and tdT-Vangl2 asymmetry across cell junctions using super-resolution (STED) imaging

We next sought to determine whether our endogenously tagged PCP lines could be used to improve resolution of Fz6 and Vangl2 asymmetry across junctions with super resolution microscopy. We recently showed that endogenous Fz6 and Vangl2 labeled with commercially available antibodies could be resolved using structured illumination microscopy (SIM) (Stahley et al., 2021). However, the 100nm maximum lateral resolution of SIM was insufficient to consistently resolve the two proteins at all junctions, especially in thicker skin samples (later than E14.5) where background and out-of-plane fluorescence interfered. Therefore, we turned to simulated emission depletion (STED) super-resolution microscopy, which can achieve less than 50nm resolution (Wegel et al., 2016). Additionally, since the Fz6 antibody epitope lies in its extracellular domain, we reasoned that fluorescent tags inserted at the cytoplasmic termini of Fz6 and Vangl2 would increase the distance between fluorescent signals and improve their resolution.

Focusing on anterior-posterior junctions that are enriched for PCP proteins, we compared standard confocal and STED microscopy on dual-labeled Fz6-3xGFP; tdTomato-Vangl2 epidermis. Even with conventional confocal imaging, some separation between the GFP and td-Tomato signal was detectable, and this was significantly improved with STED (Fig. 4B, Supplemental Figure 3A). Using STED, we observed Fz6-3xGFP and tdTomato-Vangl2 organized into punctate assemblies along A-P junctions (Fig. 4B-C Supplemental Figure 3A-B), consistent with their organization in *Drosophila* and with our previous observations using SIM (Cho et al., 2015; Stahley et al., 2021; Strutt et al., 2016; Strutt et al., 2011). We generated surface plots of Fz6-3xGFP and tdTomato-Vangl2 intensity along a junction and identified puncta as peaks of fluorescence intensity (Fig. 4D, Supplemental Figure 3C, Supplemental Video 1, peaks labeled with black and grey arrowheads). Fz6-3xGFP and tdTomato-Vangl2 puncta were often paired along A-P junctions, and we categorized puncta pairs as having an F-V or V-F orientation, depending on the position of Fz6-3xGFP (F) and tdTomato-Vangl2 (V) relative to the A-P axis. We found that the average fraction of paired puncta in the F-V orientation was higher (69.4%) than puncta in the V-F orientation (30.6%) (Fig. 4E). To test whether the F-V directional bias of puncta pairs was specific to A-P oriented junctions, we performed similar analysis on horizontally aligned, mediolateral (M-L) junctions, where PCP proteins accumulate at lower levels (see Fig. 3B-D) (Aw et al., 2016). Fz6-3xGFP and

Development • Accepted manuscript

tdTomato-Vangl2 were more diffusely localized along M-L junctions, but punctate assemblies could still be observed (Fig. 4F-H). Puncta pairs were identified (Fig. 4H, Supplemental Video 2) and categorized as having an F/V or V/F orientation relative to the M-L axis. However, we found no bias in puncta orientation relative to the M-L axis (Fig. 4I). Together these results demonstrate that super-resolution microscopy coupled with endogenously-tagged PCP protein reporters can resolve Fz6 and Vangl2 unipolar, asymmetric localizations. Moreover, these results show that although PCP protein localization is often depicted as smooth and unipolar along a junction, their submicron organization is more complex.

Live imaging in the epidermis reveals PCP asymmetry is maintained through extensive repolarization events

Basal progenitor cells of the epidermis rapidly proliferate to expand the progenitor pool and to produce the skin's suprabasal, stratified layers (Hardman et al., 1998; Muroyama and Lechler, 2012). Despite the cell shape changes in mitosis and the rearrangements accompanying daughter-cell cleavage, the asymmetry and collective alignment of PCP proteins is preserved across the tissue (Devenport et al., 2011; Shrestha et al., 2015). Using the fusion PCP reporters generated here, we were able to monitor the dynamics of PCP asymmetry through epithelial divisions and rearrangements.

To capture the dynamics of epidermal PCP, live skin explants from E15.5 Fz6-3xGFP or tdTomato-Vangl2 embryos were cultured at an air-liquid interface and z-stacks were captured every twenty minutes for approximately six hours (Fig. 5, Supplemental Figure 4, Supplemental Videos 3, 4) (Cetera et al., 2018). Both reporters displayed bright junctional labeling and minimal photobleaching. Focusing our analysis on Fz6-3xGFP, we quantified asymmetry over the entire field of view at 0, 2, 4 and 6 hour time points. Over this time period, the average orientation and magnitude of polarity across the field of view was unchanged (Fig 5A). However, when smaller, local regions of polarity were monitored over shorter time intervals, it became clear that although the global polarity of the tissue is preserved through time, the polarity of individual cells and connected groups of cells is highly dynamic (Fig. 5B, Supplemental Figure 5, Supplemental Video 5). Fluctuations in junction length and formation of multicellular vertices were associated with shifts in the direction and/or the magnitude of polarity (Supplemental Figure 5A). Cell divisions displayed the largest changes in polarity, which occurred with high

Development • Accepted manuscript

frequency. Figure 5B shows a time course of Fz6-3xGFP localization in a group of about 50 cells during which four cell divisions occur. Each cell division is associated with local shifts in Fz6-3xGFP polarity, within the dividing cell, its daughters, and in connected neighbors. Consistent with our previous observations in fixed tissue, the magnitude of polarity was diminished in mitosis and cytokinesis (Devenport et al., 2011; Heck and Devenport, 2017). Following abscission, Fz6-3xGFP asymmetry in daughter cells steadily increased (Fig. 5B-C, Supplemental Figure 5B-C). We monitored Fz6-GFP distribution across individual mitoses and found that although the angle of polarity was sometimes perfectly preserved from mother to daughter cells, other divisions resulted in significant deviation from the original polarity axis (Fig. 5C, Supplemental Figure 5B-C, Supplemental Video 6). Over time, as the polarity of some cells rotated away from the A-P axis, the polarity of other cells became better aligned with it, thereby preserving global Fz6-GFP polarity and alignment across the tissue.

Characterization of Celsr1-3xGFP, Fz6-3xGFP and tdTomato-Vangl2 in a multiciliated tissue: the adult mouse trachea

One of the best characterized functions for PCP in vertebrate systems is to direct the polarized beating of cilia in multiciliated cells (MCCs) (Meunier and Azimzadeh, 2016; Ohata and Alvarez, 2016; Wallingford and Mitchell, 2011). In mouse, MCCs produce directional fluid flow in the upper airways, the oviduct, and brain ventricles. PCP is essential for the rotational alignment of cilia basal bodies within individual MCCs, as well as for the coordinated alignment of MCC polarity across the tissue (Boutin et al., 2014; Guirao et al., 2010; Mitchell et al., 2009; Shi et al., 2014; Usami et al., 2021; Vladar et al., 2012; Vladar et al., 2015; Vladar et al., 2016). In PCP mutants, loss of directed ciliary beating results in fluid buildup in the brain (hydrocephalus), impaired airway clearance, and infertility (Ohata et al., 2014; Shi et al., 2014; Tissir et al., 2010; Vladar et al., 2012). The polarized localization of core PCP components has been well documented in the mouse trachea and in primary mouse trachea epithelial cells in culture (MTECs) (Vladar et al., 2012; Vladar et al., 2015; Vladar et al., 2016). These studies showed asymmetric localization of Vangl1 and Fz6 along the proximal-distal (P-D) axis. They further inferred from the position of Pk2 that Vangl2 is positioned on the distal side while Fz6 localizes to the proximal side (Vladar et al., 2012). Celsr1 and Vangl2 localization have not been reported in the trachea *in vivo*, but their localization in MTECs is consistent with core PCP protein distributions described in the *Drosophila* wing: Celsr1 shows bipolar asymmetry along the P-D axis whereas Vangl2 is unipolar and on the same of the cell as Pk2 (Vladar et al., 2012).

Development • Accepted manuscript

Confirming previous findings, we found that endogenously tagged Fz6-3xGFP was strongly polarized along the P-D axis in the adult trachea (Fig. 6C). Additionally, Celsr1-3xGFP showed collective alignment at P-D cell edges where it overlapped with polarized Vangl1 (Fig. 6A, Supplemental Figure 6A,B). The localization of Celsr1-3xGFP and Fz6-3xGFP were similar to their endogenous counterparts in wild-type adult trachea (Supplemental Fig. 6C,D). tdTomato-Vangl2 was also planar polarized and aligned with the P-D axis (Fig. 6B), but we were unable to label Vangl2 in wild-type trachea to compare endogenous protein localization. E-Cadherin by comparison was uniformly distributed around cell edges (Fig. 6B and Supplemental Figure 6E). Thus, similar to the polarized distribution previously reported for Fz6 and Vangl1, these data show that Celsr1 and Vangl2 are polarized in airway epithelial cells *in vivo*.

Fortuitously, in some trachea samples, our methanol fixation protocol caused the membranes of neighboring cells seperate, allowing us to clearly distinguish the proximal and distal sides of cell junctions that are normally too close together to be resolved with conventional microscopy (Fig. 6D). In trachea from Fz6-3xGFP homozygotes co-labeled with Vangl1, the two proteins showed mutually exclusive localization to opposite sides of cell junctions. Whereas Fz6-3xGFP accumulated at the proximal edges, Vangl1 localized to the distal sides. The partitioning of Fz6-3xGFP of Vangl1 was such that the two proteins displayed almost no overlap in areas where membranes had clearly separated (Fig. 6D). These findings not only confirm previous accounts of Vangl1 and Fz6 asymmetry in the trachea, they provide conclusive evidence for the unipolar localizations of Vangl1 and Fz6 to distal and proximal cell edges, respectively.

Characterization of Celsr1-3xGFP, Fz6-3xGFP and tdTomato-Vangl2 in the early embryo: neural tube and somites

Across vertebrate species, defects in the PCP pathway severely impair neural tube closure (NTC), the process by which the neural plate bends, folds and seals into a tube that gives rise to the brain and spinal cord. In mouse, PCP mutants fail to initiate NTC resulting in craniorachischisis, the most severe form of neural tube defect (NTD) (Curtin et al., 2003; Greene et al., 1998; Hamblet et al., 2002; Kibar et al., 2001b; Murdoch et al., 2001; Wang et al., 2006a; Wang et al., 2006c). Human NTD patients have been shown to carry mutations in PCP genes, including in Vangl2, Celsr1 and Fz6, closely linking the PCP pathway with human NTDs (Allache et al., 2012; De Marco et al., 2012; Juriloff and Harris, 2012; Kibar et al., 2011; Lei et al., 2010; Merello et al., 2015; Qiao et al., 2016; Wang et al., 2019). Despite the clear genetic

Development • Accepted manuscript

link between PCP and NTC in vertebrates, the subcellular localization of PCP components during neurulation is only partially understood. In *Xenopus*, Vangl2 and Prickle2 strongly enrich on the anterior side of neuroepithelial cell junctions, where their localization correlates with junction shrinkage during convergent extension movements (Butler and Wallingford, 2018). Celsr1 localizes asymmetrically to anterior-posterior cell borders in the neural-plate of chick embryos (Nishimura et al., 2012). In mouse, Vangl2 is broadly expressed in the neuroepithelium throughout neurulation but whether it is localized asymmetrically is unclear (Galea et al., 2018; Kibar et al., 2001b; Torban et al., 2008).

To address these questions, we examined Celsr1-3xGFP, Fz6-3xGFP and tdTomato-Vangl2 localization in E8.5 embryos at different A-P positions of the neural tube which close at different rates (Fig. 7 A, B). In wild-type embryos stained for the endogenous PCP proteins, similar expression patterns to the tagged proteins were observed (Supplemental Figure 7). All three fusion proteins were expressed throughout the neural tube, and were broadly localized along the lateral edges of the pseudostratified neuroepithelial cells. Notably, Celsr1-3xGFP, Fz6-3xGFP and tdTomato-Vangl2 were not enriched at the apical surface, which was marked by co-labeling with the apical, tight junction marker ZO-1. Rather, all three proteins showed reduced levels at positions of high ZO-1 accumulation (Fig. 7 C-E). Focusing on the ventral surface of still open regions of the neural tube to capture PCP protein distribution along the epithelial plane, we were unable to detect clear asymmetric localization of any of the PCP fusion proteins. Based on the extensive cell rearrangements and divisions that drive NTC, we suspect PCP asymmetries are highly dynamic and transient and may only be detectable by live imaging. Alternatively, mosaic expression of the fusion proteins may be required to reveal asymmetries of PCP proteins during neural tube development. This could be achieved by generating embryo chimeras between endogenously-tagged PCP reporter and wild-type embryos to produce mosaic expression of the tagged PCP proteins.

In imaging E8.5 embryos, we also noted that tdTomato-Vangl2 was highly expressed in the somites. Similar to its distribution in neural epithelial cells, tdTomato-Vangl2 was localized more broadly around the cell surface than ZO-1 (Fig. 7 F-H). By contrast, Celsr1-3xGFP and Fz6-3xGFP were expressed at low levels in somites, especially as compared to their levels in the neural tube midline (Fig. I-J). We saw similar expression patterns of endogenous proteins in the midline and somites of wild-type embryos, including more widespread expression of Vangl2. Thus, the neural tube defects observed in the tdTomato-Vangl2 line do not appear to be due to

Development • Accepted manuscript

aberrant expression or localization of the fusion protein (Supplemental Figure 7 F-H). Another marked difference between the three PCP proteins was their relative expression levels in the non-neural, surface ectoderm. Fz6-3xGFP levels were notably elevated in the surface ectoderm compared to other tissues at E8.5 and E9 (Supplemental Figure 7I-J). This observation is consistent with the predominant phenotype in Fz6 mutants, in which PCP defects are mainly observed in the skin epidermis. Overall, these data highlight overlapping and distinct expression patterns of the three transmembrane core PCP proteins in the early embryo, prompting us to explore their localization patterns at later stages of organogenesis.

Whole embryo imaging of Celsr1-3xGFP, Fz6-3xGFP and tdTomato-Vangl2: new patterns of expression and localization

The PCP pathway functions broadly in mammalian development in a wide range of tissues, organs and cell types (Butler and Wallingford, 2017; Wang and Nathans, 2007; Yang and Mlodzik, 2015). The insertion of fluorescent reporters into endogenous PCP loci allows investigation of the localization and dynamics of Celsr1, Fz6 and Vangl2 in any tissue where they are endogenously expressed. To explore and compare expression patterns, we surveyed Celsr1-3xGFP, Fz6-3xGFP and tdTomato-Vangl2 localization across a range of organs in sagittal sections of E16.5 embryos (Fig. 8). Overall, Celsr1-3xGFP, Fz6-3xGFP and tdTomato-Vangl2 were expressed in most epithelial tissues where they often, but not always, overlapped with E-Cadherin localization. For example, PCP fusions were coexpressed and largely colocalized with E-Cadherin in the lung, stomach, and kidney epithelia (Fig. 8A-C). By contrast, in the intestinal epithelium, PCP protein expression was more restricted. Vangl2 and Fz6 were found at the base of intestinal villi but were only weakly expressed in or absent from the rest of the epithelium. Celsr1 was detectable only in a small number of cells (of unknown identity) scattered across the intestine (Fig. 8A-C). In certain regions of the kidney tubules, the PCP fusion proteins and E-Cadherin were differentially expressed. In the liver, Fz6 was abundant and diffusely localized whereas Celsr1 and Vangl2 were only weakly expressed (Fig. 8A-C).

We also observed expression patterns unique to each transmembrane PCP protein. Celsr1 appeared to be more restricted to epithelial cell types than either Fz6 of Vangl2. By contrast, Fz6 was highly expressed in the vascular endothelium. Throughout the embryo bright Fz6-3xGFP labeling was associated with the vasculature in every organ we surveyed, including in the brain and heart (arrowheads in Fig. 8F, and Supplementary Figure 8). Perhaps most

Development • Accepted manuscript

surprising was the widespread expression of Vangl2, especially in non-epithelial cell types (Fig. 8E). tdTomato-Vangl2 was abundant in the heart, smooth muscle surrounding the digestive tract (arrows in Fig. 8E, and Supplementary Figure 8), the brain, and in stromal cells surrounding epithelial tubes like the kidney and intestine (asterisks in Fig. 8E, and Supplementary Figure 8). This broad expression pattern of Vangl2 may explain why loss-of-function mutations in Vangl2 give rise to some of the strongest embryonic phenotypes of all PCP mutants. In summary, these results demonstrate the broad utility of our endogenously-tagged, fluorescent PCP reporters to investigate PCP protein localization and function across the mouse embryo. They also suggest possible functions for PCP in the vasculature, smooth muscle and stroma of numerous organs.

Discussion

The PCP pathway regulates many facets of mammalian development, but the tools to investigate the cell biology of its core components have relied on transgenic overexpression and immunolabeling, with variable success. The three new mouse models described here, which express fluorescent Celsr1, Fz6 and Vangl2 fusion proteins from their endogenous loci, significantly improve upon existing tools for PCP protein localization and overcome many of the shortcomings associated with overexpression and immunofluorescence. We demonstrate that Celsr1-3xGFP, Fz6-3xGFP and tdTomato-Vangl2 mice are viable and show proper function and localization in the embryonic epidermis. These models enable direct visualization of PCP protein dynamics during development, and the Fz6-3xGFP and tdTomato-Vangl2 lines can be combined with super resolution imaging to localization at cell junctions. Overall, these new tools will allow for visualization of Celsr1, Fz6 and Vangl2 localization and dynamics in virtually any mouse tissue or organ where they are normally expressed.

Using endogenously tagged Fz6-3xGFP, we were able to resolve some discrepancies in the literature regarding its localization. Fz6 was initially reported to localize asymmetrically to anterior-posterior junctions in the embryonic epidermis (Devenport and Fuchs, 2008), but this was brought into question in experiments where Fz6 was overexpressed or deleted mosaically (Dong et al., 2018). Under these conditions, Dong et al. observed uniform Fz6 distribution. However, non-endogenous levels of PCP proteins have a well-documented impact on PCP signaling and mosaic overexpression or depletion of Fz can disrupt neighboring wild type cell polarity non-autonomously (Goodrich and Strutt, 2011). Our data clearly demonstrate that

Development • Accepted manuscript

endogenous Fz6-3xGFP is asymmetrically localized in epidermal cells along the anterior-posterior axis. More significantly, we show in both the epidermis and the trachea that Fz6 localization is unipolar. Using STED in the epidermis, we observe complex punctate organization of Fz6, where Fz6 is predominantly enriched on the anterior side of individual puncta pairs where it opposes Vangl2. Additionally, using methanol fixation to cause membrane separation in the trachea, we observe mutually exclusive, unipolar localization of Fz6 and Vangl1 to opposing sides of junctions. Thus, our data resolves any ambiguity in the asymmetric and opposing localization of Fz6 and Vangl1/2 in two different epithelial mammalian tissues.

Performing live imaging over six hours of epidermal development, we demonstrated that endogenously-tagged PCP reporters can be used to visualize PCP protein dynamics in living tissue and provided new insights into how polarity is maintained in the highly proliferative epidermis. These movies revealed that the local polarity of Fz6-3xGFP is constantly in flux, shifting in both orientation and magnitude as cells divide and rearrange. And yet, the average, global polarity of the tissue is preserved. We previously showed PCP is preserved during mitosis by removal of Celsr1, with associated Fz6 and Vangl2, from the cell surface via bulk internalization into membrane vesicles (Devenport et al., 2011; Shrestha et al., 2015). The proteins are held in endosomes until cytokinesis when their membrane localization and asymmetry are restored (Heck and Devenport, 2017). Our data capture the temporary loss and restoration of Fz6-3xGFP asymmetry through mitosis and cytokinesis, which had previously only been observed at fixed time points. We found that the polarity of daughter cells does not always perfectly align with that of the mother cell prior to division, suggesting that interactions with neighboring cells may be more important in directing polarity restoration after division, as opposed to the dividing cell carrying an intrinsic memory of polarity. Although the conditions required to perform long-term live imaging of the epidermis were insufficient to track endosome movements over the course of mitosis (explants are grown at an air-liquid interface, and images are captured using air objectives at 10-20 minute intervals), we believe high speed imaging of the tagged lines with immersion objectives will be possible for shorter time periods and enable high resolution imaging of PCP trafficking during mitosis.

A considerable drawback of our mouse models is the tissue-specific phenotype caused by fusing tdTomato to Vangl2. When homozygous, tdTomato-Vangl2 embryos display curly tails and neural tube closure (NTC) defects with incomplete penetrance. Yet we show that tdTomato-Vangl2 is properly localized and functional in the epidermis. One possible explanation is that the

Development • Accepted manuscript

tdTomato tag interferes with the rate of Vangl2 maturation, transport or turnover, which might be critical in highly dynamic morphogenetic processes like NTC. Alternatively, the N-terminal tag may interfere with a neural tube-specific Vangl2 protein interaction. Our favored hypothesis, however, stems from the recent discovery of an alternative, N-terminally extended form of Vangl2 which was reported during the preparation of this manuscript. Vangl2-Long is generated through an alternative translational start site and appears to be conserved in all vertebrates (Walton et al., 2020). Selective depletion of Vangl2-Long in *Xenopus* embryos resulted in severe NTC defects, potentially explaining the phenotypes we observe in our tdTomato-Vangl2 line. The N-terminal tdTomato tag is predicted to selectively block production of Vangl2-Long, which would result in loss-of-function phenotypes specifically where the Vangl2-Long isoform is expressed. Future experiments to determine where Vangl2-Long is expressed in mouse embryos will be important for determining the utility of our tdTomato-Vangl2 line. We can say with confidence that tdTomato-Vangl2 functions properly in the skin epidermis, and based on the normal morphology of other tissues that abundantly express Vangl2 it is likely that the tdTomato fusion does not interfere with Vangl2 functions in several other tissues.

Finally, using fluorescent PCP reporters to explore Celsr1, Fz6, and Vangl2 expression and localization in several embryonic tissues and organs, we identified both overlapping and unique expression patterns for each of the three transmembrane proteins, raising new questions about PCP function in mammals. For example, Fz6, but not Celsr1 or Vangl2, is highly expressed in the vasculature, suggesting it either works with other Celsr and Vang homologs in endothelial cells, or that it may have functions that are independent of PCP. Vangl2 expression is surprisingly widespread in non-epithelial tissues including smooth muscle, cardiac muscle, and stromal fibroblasts. Significantly, Celsr1 and Fz6 are not expressed in these cell types suggesting Vangl2 could be functioning independently of the core PCP pathway. There is some evidence that Vangl2 functions separately from the other PCP proteins in neurons (Dos-Santos Carvalho et al., 2020). Given that much of what we know about PCP function comes from epithelia, it will be important to decipher to what extent the principals of epithelial PCP, such as asymmetric localization and intercellular interactions at cell junctions, apply to non-epithelial tissues. Overall, these expression patterns indicate there are many unexplored functions for core PCP components in mammals. Our fluorescent PCP reporters should serve as broadly useful tools for investigating PCP localization and dynamics in a wide range of mouse tissues and organs.

Development • Accepted manuscript

Materials and Methods

Antibodies and reagents

Reagent type (species) or resource	Designation	Source or reference	Identifiers	Additional Information
Antibody	Anti-Celsr1 (Guinea pig polyclonal)	Devenport and Fuchs, 2008		1:1000
Antibody	Anti-E-cadherin, clone DECMA-1 (rat monoclonal)	Thermo Fischer	Cat #MA1-25160	1:1000 (IF, whole mount) 1:2000 (IF, sections)
Antibody	Anti-E-cadherin (rabbit monoclonal)	Cell Signaling	Cat #3195	1:250
Antibody	Anti-Vangl2 (rat monoclonal)	Millipore	Cat #MABN750	1:100
Antibody	Anti-Frizzled6 (Goat polyclonal)	R&D Biosystems	Cat #AF1526	1:400
Antibody	Anti-GFP (chicken polyclonal)	Abcam	Cat #ab6556	1:2000
Antibody	Anti-RFP (rabbit polyclonal)	Rockland Inc	Cat #600-4010379	1:200 (IF, whole mount) 1:500 (IF, sections)

Development • Accepted manuscript

Antibody	Anti-ZO-1 (rat monoclonal)	DSHB	Cat # R26.4C	1:100
Antibody	Anti-Guinea Pig, Alexa Fluor 488 (Goat)	Invitrogen	Cat #A11073	1:2000
Antibody	Anti-Guinea Pig, Alexa Fluor 647 (Donkey)	Invitrogen	Cat #A21450	1:2000
Antibody	Anti-Chicken, Alexa Fluor 488 (Goat)	Invitrogen	Cat #A-11039	1:2000
Antibody	Anti-Chicken, Alexa Fluor 488 (Donkey)	Jackson ImmunoResearch	Cat #703-545-155	1:2000
Antibody	Anti-Rabbit, Alexa Fluor 555 (Donkey)	Invitrogen	Cat #A-31572	1:2000
Antibody	Anti-Rabbit, Alexa Fluor 488 (Donkey)	Jackson ImmunoResearch	Cat #711-545-152	1:2000
Antibody	Anti-Rat, Alexa Fluor 647 (Donkey)	Jackson ImmunoResearch	Cat #712-605-153	1:2000
Antibody	Anti-Rat, Alexa Fluor 555 (Goat)	Invitrogen	Cat #A-21434	1:2000
Antibody	Anti-Rat, Alexa Fluor 488 (Donkey)	Invitrogen	Cat #A-21208	1:2000
Antibody	Anti-Goat, Alexa Fluor	Jackson ImmunoResearch	Cat #705-605-147	1:2000

Development • Accepted manuscript

	647 (Donkey)			
Antibody	Anti-chicken STAR ORANGE (goat)	Abberior	STORANGE-1005	1:100
Antibody	Anti-rabbit STAR RED (goat)	Abberior	STRED-1002	1:100
Recombinant DNA reagent	pAAV RhoB YFP Ms2	(Wilson et al., 2017)	Addgene #131777	
Recombinant DNA reagent	fat2-3xGFP floxDsRed	(Barlan et al., 2017)		
Recombinant DNA reagent	pUC vector	(Ravindran et al., 2020)		
Recombinant DNA reagent	pCAG-TAG	(Trichas et al., 2008)	Addgene #26771	
Recombinant DNA reagent	pAAV Celsr1-3xGFP	This paper		
Recombinant DNA reagent	pAAV Fz6-3xGFP	This paper		
Recombinant DNA reagent	pUC tdTomato-Vangl2	This paper		
Software, algorithm	Matlab	MathWorks	https://www.mathworks.com/products/matlab.html	
Software, algorithm	Tissue Analyzer	(Aigouy et al., 2010)	https://grr.gred-clermont.fr/labmirouse/software/WebPA/index.html	
Software, algorithm	R	R project	https://www.R-project.org/	
Software, algorithm	ggplot2	(Hadley Wickham and Thomas Lin,	https://ggplot2.tidyverse.org	

Development • Accepted manuscript

		2016)		
Software, algorithm	CaptureFigVid	MathWorks	https://www.mathworks.com/matlabcentral/fileexchange/41093-create-video-of-rotating-3d-plot	

Generation of Celsr1-3xGFP, Fz6-3xGFP and tdTomato-Vangl2 targeting constructs

To generate the Celsr1-3xGFP and Fz6-3xGFP repair constructs, a 4-kb surrounding the *Celsr1* or *Fz6* stop codons (2kb upstream and 2 kb downstream of the stop codons) were amplified from genomic DNA prepared from keratinocytes derived from CD1 mice. This sequence was inserted into the pAAV backbone to serve as homology arms (Addgene #131777, gift from the Toettcher lab) (Wilson et al., 2017) via InFusion cloning (Takara). 3xGFP was amplified (from plasmid fat2-3xGFP floxDsRed, gift from Sally Horne-Badovinac) (Barlan et al., 2017) and inserted prior to the stop codon in the homology arm constructs of Celsr1 and Fz6 through InFusion cloning.

To generate the tdTomato-Vangl2 repair constructs, homology arms of 500 bp upstream and 1-kb downstream surrounding the *Vangl2* start codon were amplified from genomic DNA from keratinocytes derived from CD1 mice. The homology arms were inserted into the pUC backbone (gift from Toettcher lab) (Ravindran et al., 2020) via InFusion cloning (Takara). tdTomato was amplified (Addgene #26771, gift from Bradley Joyce) and inserted directly following the start codon in the homology arm constructs of Vangl2 through InFusion cloning.

sgRNA target sequences were designed around the stop codon for C-terminal tagging of Celsr1 and Fz6 and the start codon for N-terminal tagging of Vangl2. Design of sgRNA and evaluation of off-target sites was done using the optimized CRISPR design tool (crispr.mit.edu). Two sgRNAs lacking predicted off-target sites in coding regions were selected for each line. If the sgRNA did not overlap with the insertion site, silent point mutations were introduced in the repair constructs. Synthetic gRNAs were either purchased from Synthego or produced in house as previously described (Gu et al., 2018).

Development • Accepted manuscript

Targeted allele	Construct design	Targeted genomic sequence with sgRNA
Celsr1-3xGFP	C-terminal fusion	**TGA**GGCACAGTCAAC**C(C→A)C**ACAG(A→G)CTGCCGGTCAAGCCCTCAGACCTT
Celsr1-3xGFP	C-terminal fusion	CCATCAGGAAA**CCATGA**GGCACAGTCAACCCCACAGACTGCCGGTCAAGC
Fz6-3xGFP	C-terminal fusion	GGGTGCTGGCAG**CCA**TTCCGACGCT**TGA**AGAAAACTGTCTCGTTCCCCCA
Fz6-3xGFP	C-terminal fusion	TGGCAGCCATT**CCG**ACGCT**TGA**AGAAAACTGTCTCGTTCCCCCAGAAGCA
tdTomato-Vangl2	N-terminal fusion	ACACACGGCGTTCGGACG**CCA**TGGACACCGAGTCCCAGTACTCGGGC
tdTomato-Vangl2	N-terminal fusion	ATGGA…TATT**C(C→A)T**ACAAGTC(G→C)GGCCACTCCCGC

Underline: sgRNA sequence, Red: stop codon, Green underline: start codon, Blue: PAM site, Dashed line: silent mutations introduced

Generation of mouse lines and breeding

Mice were housed in an AAALAC-accredited facility following the Guide for the Care and Use of Laboratory Animals. Animal maintenance and husbandry followed the laboratory Animal Welfare Act. Princeton University's Institutional Animal Care and Use Committee (IACUC) approves all animal procedures.

The Celsr-3xGFP, Fz6-3xGFP, and tdTomato-Vangl2 repair constructs (30 ng/μl), Cas9 mRNA (100 ng/μl), and sgRNA (50 ng/μl) were prepared and injected into two-cell stage CD1 mouse embryos by Eszter Posfai as previously described (Gu et al., 2020a; Gu et al., 2020b). Positive founders were determined by two sets of PCRs (described below). Founder mice were outcrossed to C57Bl/6J. N1 mice generated from these crosses were genotyped by PCR and the genomic regions spanning the homology arms were cloned into TOPO pCR4 vector (Thermofisher) and sequenced to ensure correct targeting and lack of mutations (data not shown). N1 Celsr1-3xGFP and Fz6-3xGFP mice were outcrossed to C57Bl/6J multiple times (up to five times) and N2/N3 mice were intercrossed to generate homozygotes. tdTomato-Vangl2 mice were maintained in CD1 and C57BL/6J mixed backgrounds. Although

Development • Accepted manuscript

heterozygous tdTomato-Vangl2 mice were viable and fertile, phenotypes were observed with variable penetrance when backcrossed into different backgrounds. In BL6, heterozygous mice displayed curly tails, whereas in the CD1 background, heterozygous mice displayed curly tails and hermaphroditism. Homozygous animals at postnatal stages were viable and fertile, but displayed curly tails, hermaphroditism, and head shaking behaviors.

Genotyping PCRs were designed to discriminate between WT, heterozygous, and homozygous mice for all lines. To genotype for the 3xGFP insertion, a PCR using the forward primer upstream of the 3xGFP insert and a reverse primer within the 3xGFP are used to amplify a region only in mice with the 3xGFP insertion. Similarly, a forward primer in the homology arm upstream of the insertion and a reverse primer in the tdTomato, amplify a fragment in homozygous and heterozygous knockin animals. For all three lines, a PCR using a primer upstream of the insert and downstream of the insert, amplify a large fragment in knockin animals and a small WT fragment when the insert is absent. Heterozygous animals have both large and small fragments.

PCR	Name of genotyping primer	Genotyping Primer Sequences	Where the primer binds	Product Size WT animals	Product size knockin animals
Celsr1-3xGFP insertion PCR	Celsr1.FOR	GGGTGGCCATGAATGTACGC	Upstream of 3xGFP	544 bp	2753 bp
	Celsr1.REV	CGGAGCTATGCCAGCCTTAAT	Downstream of 3xGFP		
GFP PCR	Celsr1.FOR	GGGTGGCCATGAATGTACGC	Upstream of 3xGFP	N/A	551 bp
	3xGFP.REV	CTTCATGTGGTCGGGGTAGC	Within GFP		
Fz6-3xGFP insertion PCR	Fz6.FOR	GCCTCAGTAATTGTGTCCGC	Upstream of 3xGFP	942 bp	3153 bp
	Fz6.REV	CCCTTCCCATCCCCACATTT	Downstream of 3xGFP		
GFP PCR	Fz6.FOR	GCCTCAGTAATTGTGTCCGC	Upstream of	N/A	651 bp

Development • Accepted manuscript

			3xGFP		
	3xGFP.REV	CTTCATGTGGTCGGGGTAGC	Within GFP		
tdTomato-Vangl2 insertion PCR	Vangl2.FOR	GGTATTCTCATGGAGCGCCT	Upstream of tdTomato	665 bp	2090 bp
	Vangl2.REV	TCTTTGATGACCTCCTCGCC	Downstream of tdTomato		
tdTomato PCR	Vangl2.FOR	GGTATTCTCATGGAGCGCCT	Upstream of tdTomato	N/A	331 bp
	tdTomato.REV	AAACCACTTTAGCCCCAGTGC	Within tdTomato		

Immunofluorescence and image acquisition

Embryonic Epidermis. E15.5 embryos were dissected in PBS and fixed in 4% paraformaldehyde (PFA) for 1 hour at room temperature. Backskins dissected from fixed embryos were blocked overnight at 4°C in 2% normal goat serum, 2% normal donkey serum (or 4% normal donkey serum and no goat serum when staining for Fz6), 1% bovine serum albumin and 1% fish gelatin in PBT2 (PBS with 0.2% Triton X-100). Samples were incubated in primary antibody in PBT2 overnight at 4°C, including antibodies against GFP and tdTomato as PFA fixation weakens endogenous signals. Following incubation with primary antibody, samples were washed 3 times in PBT2 for 30 minutes at room temperature and then incubated with secondary antibodies and Hoechst (Invitrogen, Cat: H1399, 1:1000) for a minimum of 2 hours at room temperature or overnight at 4°C. Samples were washed in PBT2 and PBS at room temperature and mounted in Prolong Gold.

The following primary antibodies were used: guinea pig anti-Celsr1 (Danelle Devenport, 1:1000), rat anti-E-cadherin (1:1000, DECMA-1, Thermo Fisher, Cat: MA1-25160), rabbit anti-E-cadherin (1:250, Cell Signaling: 3195), rat-anti-Vangl2 (1:100, Millipore, Cat: MABN750), goat anti-Fz6 (1:400, R&D Biosystems, Cat: AF1526), chicken anti-GFP (1:2000, Abcam, Cat: ab6556), and rabbit anti-RFP (1:200, Rockland Inc.: 600-4010379). Alexa Fluor -488, -555, and -647 secondary antibodies were used at 1:2000 (Invitrogen or Jackson ImmunoResearch).

Development • Accepted manuscript

Images were acquired on either an inverted Nikon A1 or Nikon A1R-Si confocal microscope controlled by NIS Elements software. Plan Apo 40/1.3 NA oil immersion (Nikon) objectives were used. NIS elements software, ImageJ and Photoshop were used for image processing.

Live imaging and movie processing

Live imaging of E15.5 epidermal explants was performed as previously described (Cetera et al., 2018). Briefly, E15.5 dorsal flank skin explants were dissected in PBS and mounted dermal side down onto a 1% agarose gel with F-media containing 10% fetal bovine serum. A 35-mm air permeable Lummox membrane dish (Sarstedt) was placed on the epidermal side of the skin explants. To image, explants were cultured in a humidified imaging chamber with 5% CO_2. Images were acquired using a Nikon TiE Spinning Disc with Plan Apo 20/0.75 NA air objective. Z stacks with 2 µm step sizes were acquired at 20 minute intervals for 7 hours-8 hours. Cells close to the edge of the explants were not imaged to avoid differences in planar cell polarity that could occur as a result of a wound healing response. ImageJ was used for movie processing. Drift that occurred during time-lapse imaging was corrected using the ImageJ plugin, MultiStackReg.

Image segmentation and polarity analysis

Image segmentation for the whole mount embryonic epidermis of epithelial cell edges was performed using an implementation of U-Net (Ronneberger et al., 2015), a convolutional neural network (CNN) architecture that has been shown to be very effective for image segmentation problems. For training the CNN we used 6 images of whole mount embryonic epidermis generated as described above. We separated the channels into 8-bit images of E-cadin+Vangl2, E-cadherin, Vangl2, and GFP to train the CNN on 24 total images. Post-training, one cell segmentation mask was generated using the E-cadherin marker and hand corrected using Tissue Analyzer (Aigouy et al., 2016). The masks produced from the CNN were post-processed in a MATLAB-based GUI application to produce binary masks. The post-processing included user-controlled thresholding for generating a binary mask, trimming of incomplete edges, and removing small objects leftover from thresholding. The same mask was applied as the output label for all other channels in the image.

Development • Accepted manuscript

Segmentation of live imaged Fz6-3xGFP embryonic epidermis was done using Tissue Analyzer. Segmentation of tracheal cells was done using Tissue Analyzer and E-cadherin to mark cell edges (Aigouy et al., 2010).

Polarity was calculated using Packing Analyzer V2 software as previously described (Aigouy et al., 2010). The software calculates the axis and magnitude (nematic order) of PCP protein distribution along cell edges, which are defined by binary masks generated by automated segmentation as described above. Data were plotted in circular histograms using MATLAB. The average polarity magnitude, as defined in Aigouy et al., 2016 (Aigouy et al., 2016), was plotted on the circular histograms to indicate both angle and strength of polarity. Prior to polarity analysis, images were rotated up to 15 degrees to align them with the anterior-posterior axis.

STED imaging and image analysis

E15.5 backskins were dissected, fixed and stained as described above. Primary antibodies used were chicken anti-GFP (1:2000, Abcam, Cat: ab6556), and rabbit ant-RFP (1:200, Rockland Inc.: 600-4010379). Samples were incubated in secondary in PBT2 overnight at 4°C. Secondary antibodies used were goat anti-chicken STAR ORANGE (1:100, Abberior: STORANGE-1005) and goat anti-rabbit STAR RED (1:100, Abberior: STRED-1002). Skins were mounted in Prolong Gold.

Images were acquired using a Nikon A1R-HD25 confocal microscope coupled to an inverted Ti-2 stand with a STEDYCON stimulated emission depletion (STED) module. STED images were acquired with a Plan Apo 100X 1.49 NA oil-immersion objective (Nikon). Z-stacks were acquired with 0.25 µm steps. NIS elements software, NIS-Elements AR analysis, ImageJ and Adobe Photoshop were used for image deconvolution and processing.

XY resolution for the STARRED and STARORANGE antibodies was acquired by imaging single molecules of the secondary antibodies smeared on a slide and mounted in Prolong Gold, similarly to our epidermis samples. We determined the point spread function of the signal from single molecules of antibody. We found an average FWHM across 12 molecules of 48.7 nm in the X axis and an average of 51.1 nm in the Y axis for the STARRED antibody. The STARORANGE antibody showed a reduction in resolution, with an average of 57.8 nm in the X

Development • Accepted manuscript

axis and 59.1 nm in the Y axis across 17 molecules. Based on these values, our following analyses assume a XY resolution of 65 nm.

Binary masks were generated in Fiji in order to identify the junctions for analysis and exclude any obvious cytoplasmic signal. These masks along with images of full junctions were acquired and imported into MATLAB 2021a for analysis, with masks being applied to full junction images by image multiplication. To identify the center of puncta, the imregionalmax function was used to identify local maxima in the image. Local maxima which were below three standard deviations of the mean intensity of the image were filtered out. Peaks within 3.25 pixels (resolution divided by pixel size) of another peak of the same channel were combined by averaging their x and y-coordinates and intensity values. Puncta of Fz6-3xGFP and tdTomato-Vangl2 peaks were then paired, with a cut off of 220 nm, to account for peaks with no obvious corresponding peak of the other channel. A given peak can be paired with any number of peaks from the other channel, however, pairs are unique. All MATLAB scripts are available on request.

Orientation of pairs relative to the junction orientation were then calculated. This orientation was defined by either the relative x-coordinate for vertical junctions or y-coordinate for horizontal junctions. For vertical junctions, if the x-coordinate of the Fz6-3xGFP peak was less than or equal to that of the tdTomato-Vangl2, it was defined as being in the FV orientation. If greater than, then the pair was defined as being in the VF orientation. For horizontal junctions, if the y-coordinate of the Fz6-3xGFP peak was greater than or equal to that of the tdTomato-Vangl2, it was defined as being in the V/F orientation. If less than, then the pair was defined as being in the F/V orientation.

To further visualize this STED microscopy data, for both stained channels, image intensity values were stretched to saturate the bottom and top 1% of pixel values using the imadjust function in MATLAB, to increase contrast. This adjusted image data was then used to generate a surface plot for each image using the surf function in MATLAB. The previously calculated peaks were then plotted on the surface plots using the scatter3 function in MATLAB. To aid in visualization, each point on the surface plot was assigned a transparency based on its corresponding pixel intensity, low values had high transparency, and high values had low transparency. Rotating videos of these plots were generated using the CaptureFigVid package (Jennings, 2021).

Development • Accepted manuscript

Trachea dissection and immunostaining

Tracheas were dissected from adult mice and fixed in 100% methanol at -20°C for 10 minutes or in 4% paraformaldehyde (PFA) for 1 hour at 4°C. Tracheas were then washed in PBS, blocked overnight in 4% normal donkey serum, 1% bovine serum albumin and 1% fish gelatin in PBT2 (PBS with 0.2% Triton X-100). Traches were incubated with primary antibody in blocking buffer overnight at 4°C, washed with PBT2 at room temperature, incubated with secondary antibody overnight, and then washed in PBT2 followed by PBS and mounted in Prolong Gold. GFP and tdTomato were stained against as trachea fixation in methanol and PFA weakens the endogenous signal of both GFP and tdTomato.

Images were acquired on either an inverted Nikon A1 or Nikon A1R-Si confocal microscope controlled by NIS Elements software. Plan Apo 40/1.3 NA oil immersion (Nikon) and Plan Apo 60X 1.40 NA oil immersion (Nikon) objectives were used. NIS elements software, ImageJ and Photoshop were used for image processing.

Neural tube E8.5 immunostaining

E8.5 embryos were dissected in M2 media as previously described (Xiao et al., 2018). Briefly, the pregnant female was sacrificed, E8.5 embryos were removed from the abdomen, and uterine muscles were removed to free the decidua. A longitudinal incision through the decidua was made to separate the embryo from the future placenta. A portion of the yolk sac was removed for genotyping. E8.5 Embryos were fixed in 4% paraformaldehyde for 45 minutes at room temperature and blocked overnight at 4°C in 2% normal goat serum, 2% normal donkey serum (or 4% normal donkey serum and no goat serum when staining for Fz6), 1% bovine serum albumin and 1% fish gelatin in PBT2 (PBS with 0.2% Triton X-100). Samples were incubated in primary antibody in PBT2 overnight at 4°C. Following incubation with primary antibody, samples were washed in PBT2 room temperature and then incubated with secondary antibodies and Hoechst (Invitrogen, Cat: H1399, 1:1000) overnight at 4°C. Samples were washed in PBT2 and PBS at room temperature and mounted in Prolong Gold.

Development • Accepted manuscript

The following primary antibodies were used: chicken anti-GFP (1:2000, Abcam, Cat: ab6556), rabbit ant-RFP (1:200, Rockland Inc.: 600-4010379), and rat anti-ZO-1 (1:100, DSHB: R26.4C).

Images were acquired on an inverted Nikon A1 confocal microscope controlled by NIS Elements software. Plan Apo 40/1.3 NA oil immersion (Nikon) objectives were used. Images were acquired using 1 μm z-steps. NIS elements software, ImageJ and Photoshop were used for image processing.

E16.5 embedding, sectioning, and staining

E16.5 embryos were dissected in PBS by removing the tail for genotyping and making 3-5 mm incisions on the ventral side of the embryo to expose internal organs. Embryos were fixed in 4% paraformaldehyde for 1.5 hours at 4°C, washed three times in PBS for at least 15 minutes at 4°C, and then washed additionally in PBS overnight at 4°C. Embryos were infused with 20% sucrose in PBS for 1 hour at 4°C, in 30% sucrose in PBS for 1 hour at 4°C, in 1:1 30% sucrose:OCT for 1 hour at 4°C, and lastly in 1:1 30% sucrose:OCT overnight at 4°C. Embryos were embedded in OCT on dry ice and stored at -80°C.

Frozen OCT-embedded embryos were cryosectioned on a Leica CM3050 cryostat. Full embryo, sagittal sections were cut at 10um thickness, collected on Superfrost Plus coated slides and allowed to dry for at least 30 minutes prior to being stored at -20°C.

For immunostaining, sections were rehydrated for 10 minutes in PBS at room temperature in a humidified chamber on a flat surface, permeabilized in PBT (PBS with 0.1% Triton X-100) for 10 minutes at room temperature, and blocked in 2% normal goat serum, 2% normal donkey serum, and 2% bovine serum album in PBT for 1 hour at room temperature. Slides were incubated with primary antibody in block for 1 hour at room temperature: rat anti-E-cadherin (1:2000, DECMA-1, Thermo Fisher, Cat: MA1-25160), chicken anti-GFP (1:2000, Abcam, Cat: ab6556), and rabbit ant-RFP (1:500, Rockland Inc.: 600-4010379). Slides were washed three times for 10 minutes with PBT and incubated with secondary antibodies in PBT for 1 hour at room temperature. Alexa Fluor -488, -555, and -647 secondary antibodies and were used at 1:2000 (Invitrogen). Slides were washed in PBT with Hoechst (Invitrogen, Cat: H1399, 1:2000) for 10 minutes, followed by two 10 minutes washes in PBT. A final wash in PBS for 10 minutes was

Development • Accepted manuscript

done prior to mounting in glycerol-based mounting media (90% glycerol in PBS) with anti-fade reagent and sealed with nail polish. Slides were stored at -20°C.

Images were acquired on either an inverted Nikon A1R-Si or a Nikon A1R-HD25 confocal microscope controlled by NIS Elements software. Plan Apo 60X 1.40 NA oil immersion (Nikon) objectives were used. When acquiring large tissue areas, 5x5 or larger XY regions were collected using resonance scanning with 16x averaging. Images were denoised and stitched together with 15% overlap using NIS elements software. ImageJ and Photoshop were used for further image processing.

Author Contributions

Lena P. Basta performed experiments, analyzed data, and wrote the manuscript. Michael Hill-Oliva contributed to initial characterization of the mouse lines. Sarah V. Paramore performed trachea experiments. Rishabh Sharan contributed to quantitative data analysis of STED results. Audrey Goh contributed to polarity analysis of the epidermal skin. Abhishek Biswas developed the 2D segmentation software for polarity analysis of the epidermis. Marvin Cortez assisted in the dissection and characterization of E8.5 embryos. Katherine A. Little performed embedding of E16.5 embryos for sectioning and staining of sections. Eszter Posfai consulted on the 2C-HR-CRISPR design strategy and performed 2-cell embryo injections and transfers to generate the mouse lines. Danelle Devenport oversaw the experimental design and analysis, sectioned and imaged E16.5 sections, and wrote the manuscript.

Acknowledgements: The authors thank all those who provided resources, technical support and valuable discussions that contributed to this work. We thank all Devenport lab members for their feedback and advice, especially Liliya Leybova for her help with dissections and experimental set up. We particularly acknowledge technical support from the Model Production Core staff led by M. Gertsenstein at the Centre for Phenogenomics, Toronto. We thank Pavithran T. Ravindran for his help in construct design and cloning assistance. We thank Gary Laevsky in the Princeton University Confocal Imaging Facility, a Nikon Center of Excellence, for imaging support, expertise, and assistance. This work was supported by the National Institute of Arthritis and Musculoskeletal and Skin Diseases under grant numbers R01 AR066070, R01 AR068320 and F31 AR077407 and National Institute of General Medical Science of the National Institute of Health under grant number T32GM007388.

Development • Accepted manuscript

References

Adler, P. N. (2012). The frizzled/stan pathway and planar cell polarity in the Drosophila wing. *Current topics in developmental biology* **101**, 1-31.

Adler, P. N. and Lee, H. (2001). Frizzled signaling and cell-cell interactions in planar polarity. *Current opinion in cell biology* **13**, 635-640.

Adler, P. N. and Wallingford, J. B. (2017). From Planar Cell Polarity to Ciliogenesis and Back: The Curious Tale of the PPE and CPLANE proteins. *Trends in cell biology* **27**, 379-390.

Aigouy, B., Farhadifar, R., Staple, D. B., Sagner, A., Röper, J. C., Jülicher, F. and Eaton, S. (2010). Cell flow reorients the axis of planar polarity in the wing epithelium of Drosophila. *Cell* **142**, 773-786.

Aigouy, B., Umetsu, D. and Eaton, S. (2016). Segmentation and Quantitative Analysis of Epithelial Tissues. *Methods in molecular biology (Clifton, N.J.)* **1478**, 227-239.

Allache, R., De Marco, P., Merello, E., Capra, V. and Kibar, Z. (2012). Role of the planar cell polarity gene CELSR1 in neural tube defects and caudal agenesis. *Birth defects research. Part A, Clinical and molecular teratology* **94**, 176-181.

Apodaca, G. (2018). Role of Polarity Proteins in the Generation and Organization of Apical Surface Protrusions. *Cold Spring Harbor perspectives in biology* **10**, 1-33.

Aw, W. Y., Heck, B. W., Joyce, B. and Devenport, D. (2016). Transient Tissue-Scale Deformation Coordinates Alignment of Planar Cell Polarity Junctions in the Mammalian Skin. *Current biology : CB* **26**, 2090-2100.

Bailly, E., Walton, A. and Borg, J. (2018). The planar cell polarity Vangl2 protein: From genetics to cellular and molecular functions. *Seminars in cell & developmental biology* **81**, 62-70.

Barlan, K., Cetera, M. and Horne-Badovinac, S. (2017). Fat2 and Lar Define a Basally Localized Planar Signaling System Controlling Collective Cell Migration. *Developmental cell* **40**, 467-477.

Development • Accepted manuscript

Boutin, C., Labedan, P., Dimidschstein, J., Richard, F., Cremer, H., André, P., Yang, Y., Montcouquiol, M., Goffinet, A. M. and Tissir, F. (2014). A dual role for planar cell polarity genes in ciliated cells. *Proceedings of the National Academy of Sciences of the United States of America* **111**, E3129-3138.

Butler, M. T. and Wallingford, J. B. (2015). Control of vertebrate core planar cell polarity protein localization and dynamics by Prickle 2. *Development* **142**, 3429-3439.

Butler, M. T. and Wallingford, J. B. (2017). Planar cell polarity in development and disease. *Nature reviews. Molecular cell biology* **18**, 375-388.

Butler, M. T. and Wallingford, J. B. (2018). Spatial and temporal analysis of PCP protein dynamics during neural tube closure. *eLife* **7**, e36456.

Cai, C. and Shi, S. (2014). Genetic evidence in planar cell polarity signaling pathway in human neural tube defects. *Frontiers of medicine* **8**, 68-78.

Carroll, T. J. and Yu, J. (2012). The kidney and planar cell polarity. *Current topics in developmental biology* **101**, 185-212.

Carvajal-Gonzalez, J. M. and Mlodzik, M. (2014). Mechanisms of planar cell polarity establishment in Drosophila. *F1000prime reports* **6**, 1-10.

Cetera, M., Leybova, L., Joyce, B. and Devenport, D. (2018). Counter-rotational cell flows drive morphological and cell fate asymmetries in mammalian hair follicles. *Nature cell biology* **20**, 541-552.

Cetera, M., Leybova, L., Woo, F. W., Deans, M. and Devenport, D. (2017). Planar cell polarity-dependent and independent functions in the emergence of tissue-scale hair follicle patterns. *Developmental biology* **428**, 188-203.

Chang, H., Smallwood, P. M., Williams, J. and Nathans, J. (2016). The spatio-temporal domains of Frizzled6 action in planar polarity control of hair follicle orientation. *Developmental biology* **409**, 181-193.

Chien, Y. H., Keller, R., Kintner, C. and Shook, D. R. (2015). Mechanical strain determines the axis of planar polarity in ciliated epithelia. *Current biology : CB* **25**, 2774-2784.

Development • Accepted manuscript

Cho, B., Pierre-Louis, G., Sagner, A., Eaton, S. and Axelrod, J. D. (2015). Clustering and negative feedback by endocytosis in planar cell polarity signaling is modulated by ubiquitinylation of prickle. *PLoS genetics* **11**, e1005259.

Curtin, J. A., Quint, E., Tsipouri, V., Arkell, R. M., Cattanach, B., Copp, A. J., Henderson, D. J., Spurr, N., Stanier, P., Fisher, E. M., et al. (2003). Mutation of Celsr1 disrupts planar polarity of inner ear hair cells and causes severe neural tube defects in the mouse. *Current biology : CB* **13**, 1129-1133.

De Marco, P., Merello, E., Piatelli, G., Cama, A., Kibar, Z. and Capra, V. (2014). Planar cell polarity gene mutations contribute to the etiology of human neural tube defects in our population. *Birth defects research. Part A, Clinical and molecular teratology* **100**, 633-641.

De Marco, P., Merello, E., Rossi, A., Piatelli, G., Cama, A., Kibar, Z. and Capra, V. (2012). FZD6 is a novel gene for human neural tube defects. *Human mutation* **33**, 384-390.

Devenport, D. (2014). The cell biology of planar cell polarity. *The Journal of cell biology* **207**, 171-179.

Devenport, D. (2016). Tissue morphodynamics: Translating planar polarity cues into polarized cell behaviors. *Seminars in cell & developmental biology* **55**, 99-110.

Devenport, D. and Fuchs, E. (2008). Planar polarization in embryonic epidermis orchestrates global asymmetric morphogenesis of hair follicles. *Nature cell biology* **10**, 1257-1268.

Devenport, D., Oristian, D., Heller, E. and Fuchs, E. (2011). Mitotic internalization of planar cell polarity proteins preserves tissue polarity. *Nature cell biology* **13**, 893-902.

Dong, B., Vold, S., Olvera-Jaramillo, C. and Hao, C. (2018). Functional redundancy of frizzled 3 and frizzled 6 in planar cell polarity control of mouse hair follicles. *Development* **145**, dev168468.

Dos-Santos Carvalho, S., Moreau, M. M., Hien, Y. E., Garcia, M., Aubailly, N., Henderson, D. J., Studer, V., Sans, N., Thoumine, O. and Montcouquiol, M. (2020). Vangl2 acts at the interface between actin and N-cadherin to modulate mammalian neuronal outgrowth. *eLife* **9**, e51822.

Development • Accepted manuscript

Ezan, J. and Montcouquiol, M. (2013). Revisiting planar cell polarity in the inner ear. *Seminars in cell & developmental biology* **24**, 499-506.

Galea, G. L., Nychyk, O., Mole, M. A., Moulding, D., Savery, D., Nikolopoulou, E., Henderson, D. J., Greene, N. D. E. and Copp, A. J. (2018). Vangl2 disruption alters the biomechanics of late spinal neurulation leading to spina bifida in mouse embryos. *Disease models & mechanisms* **11**, dmm032219.

Goodrich, L. V. and Strutt, D. (2011). Principles of planar polarity in animal development. *Development (Cambridge, England)* **138**, 1877-1892.

Greene, N. D., Gerrelli, D., Van Straaten, H. W. and Copp, A. J. (1998). Abnormalities of floor plate, notochord and somite differentiation in the loop-tail (Lp) mouse: a model of severe neural tube defects. *Mechanisms of development* **73**, 59-72.

Gu, B., Gertsenstein, M. and Posfai, E. (2020a). Generation of Large Fragment Knock-In Mouse Models by Microinjecting into 2-Cell Stage Embryos. *Methods in molecular biology (Clifton, N.J.)* **2066**, 89-100.

Gu, B., Posfai, E., Gertsenstein, M. and Rossant, J. (2020b). Efficient Generation of Large-Fragment Knock-In Mouse Models Using 2-Cell (2C)-Homologous Recombination (HR)-CRISPR. *Current protocols in mouse biology* **10**, e67.

Gu, B., Posfai, E. and Rossant, J. (2018). Efficient generation of targeted large insertions by microinjection into two-cell-stage mouse embryos. *Nature biotechnology* **36**, 632-637.

Guirao, B., Meunier, A., Mortaud, S., Aguilar, A., Corsi, J. M., Strehl, L., Hirota, Y., Desoeuvre, A., Boutin, C., Han, Y. G., et al. (2010). Coupling between hydrodynamic forces and planar cell polarity orients mammalian motile cilia. *Nature cell biology* **12**, 341-350.

Guo, N., Hawkins, C. and Nathans, J. (2004). Frizzled6 controls hair patterning in mice. *PNAS* **101**, 9277-9281.

Hadley Wickham, D. N. and Thomas Lin, P. (2016). *ggplot2: Elegant Graphics for Data Analysis* (1 edn). New York, USA: Springer International Publishing.

Development • Accepted manuscript

Hamblet, N. S., Lijam, N., Ruiz-Lozano, P., Wang, J., Yang, Y., Luo, Z., Mei, L., Chien, K. R., Sussman, D. J. and Wynshaw-Boris, A. (2002). Dishevelled 2 is essential for cardiac outflow tract development, somite segmentation and neural tube closure. *Development (Cambridge, England)* **129**, 5827-5838.

Hardman, M. J., Sisi, P., Banbury, D. N. and Byrne, C. (1998). Patterned acquisition of skin barrier function during development. *Development (Cambridge, England)* **125**, 1541-1552.

Harrison, C., Shao, H., Strutt, H. and Strutt, D. (2020). Molecular mechanisms mediating asymmetric subcellular localisation of the core planar polarity pathway proteins. *Biochemical Society transactions* **48**, 1297-1308.

Heck, B. W. and Devenport, D. (2017). Trans-endocytosis of Planar Cell Polarity Complexes during Cell Division. *Current biology : CB* **27**, 3725-3733.

Huebner, R. J. and Wallingford, J. B. (2018). Coming to Consensus: A Unifying Model Emerges for Convergent Extension. *Developmental cell* **46**, 389-396.

Iwasaki, M., Kuroda, J., Kawakami, K. and Wada, H. (2018). Epidermal regulation of bone morphogenesis through the development and regeneration of osteoblasts in the zebrafish scale. *Developmental biology* **437**, 105-119.

Jennings, A. (2021). Create Video of Rotating 3D Plot. MATLAB Central File Exchange.

Jones, C. and Chen, P. (2007). Planar cell polarity signaling in vertebrates. *BioEssays : news and reviews in molecular, cellular and developmental biology* **29**, 120-132.

Juriloff, D. M. and Harris, M. J. (2012). A consideration of the evidence that genetic defects in planar cell polarity contribute to the etiology of human neural tube defects. *Birth defects research. Part A, Clinical and molecular teratology* **94**, 824-840.

Jussila, M. and Ciruna, B. (2017). Zebrafish models of non-canonical Wnt/planar cell polarity signalling: fishing for valuable insight into vertebrate polarized cell behavior. *Wiley interdisciplinary reviews. Developmental biology* **6**, e267.

Kibar, Z., Salem, S., Bosoi, C. M., Pauwels, E., De Marco, P., Merello, E., Bassuk, A. G., Capra, V. and Gros, P. (2011). Contribution of VANGL2 mutations to isolated neural tube defects. *Clinical genetics* **80**, 76-82.

Development • Accepted manuscript

Kibar, Z., Underhill, D. A., Canonne-Hergaux, F., Gauthier, S., Justice, M. J. and Gros, P. (2001a). Identification of a new chemically induced allele (Lp(m1Jus)) at the loop-tail locus: morphology, histology, and genetic mapping. *Genomics* **72**, 331-337.

Kibar, Z., Vogan, K. J., Groulx, N., Justice, M. J., Underhill, D. A. and Gros, P. (2001b). Ltap, a mammalian homolog of Drosophila Strabismus/Van Gogh, is altered in the mouse neural tube mutant Loop-tail. *Nature genetics* **28**, 251-255.

Lei, Y. P., Zhang, T., Li, H., Wu, B. L., Jin, L. and Wang, H. Y. (2010). VANGL2 mutations in human cranial neural-tube defects. *The New England journal of medicine* **362**, 2232-2235.

Matis, M., Russler-Germain, D. A., Hu, Q., Tomlin, C. J. and Axelrod, J. D. (2014). Microtubules provide directional information for core PCP function. *eLife* **3**, e02893.

Maung, S. M. T. W. and Jenny, A. (2011). Planar cell polarity in Drosophila. *Organogenesis* **7**, 165-179.

Merello, E., Mascelli, S., Raso, A., Piatelli, G., Consales, A., Cama, A., Kibar, Z., Capra, V. and De Marco, P. (2015). Expanding the mutational spectrum associated to neural tube defects: literature revision and description of novel VANGL1 mutations. *Birth defects research. Part A, Clinical and molecular teratology* **103**, 51-61.

Meunier, A. and Azimzadeh, J. (2016). Multiciliated Cells in Animals. *Cold Spring Harbor perspectives in biology* **8**, a028233.

Mitchell, B., Stubbs, J. L., Huisman, F., Taborek, P., Yu, C. and Kintner, C. (2009). The PCP pathway instructs the planar orientation of ciliated cells in the Xenopus larval skin. *Current biology* **19**, 924-929.

Murdoch, J. N., Doudney, K., Paternotte, C., Copp, A. J. and Stanier, P. (2001). Severe neural tube defects in the loop-tail mouse result from mutation of Lpp1, a novel gene involved in floor plate specification. *Human molecular genetics* **10**, 2593-2601.

Muroyama, A. and Lechler, T. (2012). Polarity and stratification of the epidermis. *Seminars in cell & developmental biology* **23**, 890-896.

Nikolopoulou, E., Galea, G. L., Rolo, A., Greene, N. D. and Copp, A. J. (2017). Neural tube closure: cellular, molecular and biomechanical mechanisms. *Development* **144**, 552-566.

Development • Accepted manuscript

Nishimura, T., Honda, H. and Takeichi, M. (2012). Planar Cell Polarity Links Axes of Spatial Dynamics in Neural-Tube Closure. *Cell* **149**, 1084-1097.

Ohata, S. and Alvarez, B. (2016). Planar Organization of Multiciliated Ependymal (E1) Cells in the Brain Ventricular Epithelium. *Trends in neurosciences* **39**, 543-551.

Ohata, S., Nakatani, J., Herranz-Pérez, V., Cheng, J., Belinson, H., Inubushi, T., Snider, W. D., García-Verdugo, J. M., Wynshaw-Boris, A. and Alvarez-Buylla, A. (2014). Loss of Dishevelleds disrupts planar polarity in ependymal motile cilia and results in hydrocephalus. *Neuron* **83**, 558-571.

Olofsson, J. and Axelrod, J. D. (2014). Methods for studying planar cell polarity. *Methods (San Diego, Calif.)* **68**, 97-104.

Park, M. and Moon, R. T. (2002). The planar cell-polarity gene stbm regulates cell behaviour and cell fate in vertebrate embryos. *Nature cell biology* **4**, 20-25.

Qiao, X., Liu, Y., Li, P., Chen, Z., Li, H., Yang, X., Finnell, R. H., Yang, Z., Zhang, T., Qiao, B., et al. (2016). Genetic analysis of rare coding mutations of CELSR1-3 in congenital heart and neural tube defects in Chinese people. *Clinical science (London, England : 1979)* **130**, 2329-2340.

Ravindran, P. T., Wilson, M. Z., Jena, S. G. and Toettcher, J. E. (2020). Engineering combinatorial and dynamic decoders using synthetic immediate-early genes. *Communications biology* **3**, 436.

Ravni, A., Qu, Y., Goffinet, A. M. and Tissir, F. (2009). Planar cell polarity cadherin Celsr1 regulates skin hair patterning in the mouse. *The Journal of investigative dermatology* **129**, 2507-2509.

Ronneberger, O., Fischer, P. and Brox, T. (2015). U-Net: Convolutional Networks for Biomedical Image Segmentation | SpringerLink. In *Medical Image Computing and Computer-Assisted Intervention – MICCAI 2015*: Springer, Cham.

Schweisguth, F. (2015). Asymmetric cell division in the Drosophila bristle lineage: from the polarization of sensory organ precursor cells to Notch-mediated binary fate decision. *Wiley interdisciplinary reviews. Developmental biology* **4**, 299-309.

Development • Accepted manuscript

Segalen, M. and Bellaïche, Y. (2009). Cell division orientation and planar cell polarity pathways. *Seminars in cell & developmental biology* **20**, 972-977.

Shi, D., Komatsu, K., Hirao, M., Toyooka, Y., Koyama, H., Tissir, F., Goffinet, A. M., Uemura, T. and Fujimori, T. (2014). Celsr1 is required for the generation of polarity at multiple levels of the mouse oviduct. *Development* **141**, 4558-4568.

Shi, D., Usami, F., Komatsu, K., Oka, S., Abe, T., Uemura, T. and Fujimori, T. (2016). Dynamics of planar cell polarity protein Vangl2 in the mouse oviduct epithelium. *Mechanisms of development* **141**, 78-89.

Shimada, Y., Yonemura, S., Ohkura, H., Strutt, D. and Uemura, T. (2006). Polarized transport of Frizzled along the planar microtubule arrays in Drosophila wing epithelium. *Developmental cell* **10**, 209-222.

Shindo, A., Audrey, A., Takagishi, M., Takahashi, M., Wallingford, J. B. and Kinoshita, M. (2018). Septin-dependent remodeling of cortical microtubule drives cell reshaping during epithelial wound healing. *Journal of cell science* **131**, jcs212647.

Shrestha, R., Little, K. A., Tamayo, J. V., Li, W., Perlman, D. H. and Devenport, D. (2015). Mitotic Control of Planar Cell Polarity by Polo-like Kinase 1. *Developmental cell* **33**, 522-534.

Stahley, S. N., Basta, L. P., Sharan, R. and Devenport, D. (2021). Celsr1 adhesive interactions mediate the asymmetric organization of planar polarity complexes. *elife* **10**, e62097.

Strutt, H., Gamage, J. and Strutt, D. (2016). Robust Asymmetric Localization of Planar Polarity Proteins Is Associated with Organization into Signalosome-like Domains of Variable Stoichiometry. *Cell reports* **17**, 2660-2671.

Strutt, H. and Strutt, D. (2009). Asymmetric localisation of planar polarity proteins: Mechanisms and consequences. *Seminars in cell & developmental biology* **20**, 957-963.

Strutt, H., Warrington, S. J. and Strutt, D. (2011). Dynamics of core planar polarity protein turnover and stable assembly into discrete membrane subdomains. *Developmental cell* **20**, 511-525.

Sutherland, A., Keller, R. and Lesko, A. (2020). Convergent extension in mammalian morphogenesis. *Seminars in cell & developmental biology* **100**, 199-211.

Development • Accepted manuscript

Tada, M. and Heisenberg, C. (2012). Convergent extension: using collective cell migration and cell intercalation to shape embryos. *Development* **139**, 3897-3904.

Team, R. C. (2021). R: The R Project for Statistical Computing.

Tissir, F., Qu, Y., Montcouquiol, M., Zhou, L., Komatsu, K., Shi, D., Fujimori, T., Labeau, J., Tyteca, D., Courtoy, P., et al. (2010). Lack of cadherins Celsr2 and Celsr3 impairs ependymal ciliogenesis, leading to fatal hydrocephalus. *Nature neuroscience* **13**, 700-707.

Torban, E., Patenaude, A. M., Leclerc, S., Rakowiecki, S., Gauthier, S., Andelfinger, G., Epstein, D. J. and Gros, P. (2008). Genetic interaction between members of the Vangl family causes neural tube defects in mice. *Proceedings of the National Academy of Sciences of the United States of America* **105**, 3449-3454.

Torban, E., Wang, H. J., Groulx, N. and Gros, P. (2004). Independent mutations in mouse Vangl2 that cause neural tube defects in looptail mice impair interaction with members of the Dishevelled family. *The Journal of biological chemistry* **279**, 52703-52713.

Trichas, G., Begbie, J. and Srinivas, S. (2008). Use of the viral 2A peptide for bicistronic expression in transgenic mice. *BMC biology* **6**.

Usami, F. M., Arata, M., Shi, D., Oka, S., Higuchi, Y., Tissir, F., Takeichi, M. and Fujimori, T. (2021). Intercellular and intracellular cilia orientation is coordinated by CELSR1 and CAMSAP3 in oviduct multi-ciliated cells. *Journal of cell science* **134**, jcs257006.

Vladar, E. K., Bayly, R. D., Sangoram, A. M., Scott, M. P. and Axelrod, J. D. (2012). Microtubules enable the planar cell polarity of airway cilia. *Current biology* **22**, 2203-2212.

Vladar, E. K., Lee, Y. L., Stearns, T. and Axelrod, J. D. (2015). Observing planar cell polarity in multiciliated mouse airway epithelial cells. *Methods in cell biology* **127**, 37-54.

Vladar, E. K., Nayak, J. V., Milla, C. E. and Axelrod, J. D. (2016). Airway epithelial homeostasis and planar cell polarity signaling depend on multiciliated cell differentiation. *JCI insight* **1**, e88027.

Wallingford, J. B. (2012). Planar cell polarity and the developmental control of cell behavior in vertebrate embryos. *Annual review of cell and developmental biology* **28**, 627-653.

Development • Accepted manuscript

Wallingford, J. B. and Mitchell, B. (2011). Strange as it may seem: the many links between Wnt signaling, planar cell polarity, and cilia. *Genes & development* **25**, 201-213.

Walton, A., Revinski, D., Sergé, A., Audebert, S., Camoin, L., Puvirajesinghe, T. M., Isnardon, D., Marchetto, S., Kodjabachian, L., Bailly, E., et al. (2020). A novel Golgi-associated Vangl2 translational variant required for PCP regulation in vertebrates. *bioRxiv*.

Wang, J., Hamblet, N. S., Mark, S., Dickinson, M. E., Brinkman, B. C., Segil, N., Fraser, S. E., Chen, P., Wallingford, J. B. and Wynshaw-Boris, A. (2006a). Dishevelled genes mediate a conserved mammalian PCP pathway to regulate convergent extension during neurulation. *Development* **133**, 1767-1778.

Wang, M., Marco, P., Capra, V. and Kibar, Z. (2019). Update on the Role of the Non-Canonical Wnt/Planar Cell Polarity Pathway in Neural Tube Defects. *Cells* **8**, 1198.

Wang, Y., Badea, T. and Nathans, J. (2006b). Order from disorder: Self-organization in mammalian hair patterning. *Proceedings of the National Academy of Sciences of the United States of America* **103**, 19800-19805.

Wang, Y., Chang, H. and Nathans, J. (2010). When whorls collide: the development of hair patterns in frizzled 6 mutant mice. *Development (Cambridge, England)* **137**, 4091-4099.

Wang, Y., Guo, N. and Nathans, J. N. (2006c). The role of Frizzled3 and Frizzled6 in neural tube closure and in the planar polarity of inner-ear sensory hair cells. *The Journal of neuroscience : the official journal of the Society for Neuroscience* **26**, 2147-2156.

Wang, Y. and Nathans, J. (2007). Tissue/planar cell polarity in vertebrates: new insights and new questions. *Development* **134**, 647-658.

Wegel, E., Göhler, A., Lagerholm, B. C., Wainman, A., Uphoff, S., Kaufmann, R. and Dobbie, I. M. (2016). Imaging cellular structures in super-resolution with SIM, STED and Localisation Microscopy: A practical comparison. *Scientific reports* **6**.

Wilson, M. Z., Ravindran, P. T., Lim, W. A. and Toettcher, J. E. (2017). Tracing Information Flow from Erk to Target Gene Induction Reveals Mechanisms of Dynamic and Combinatorial Control. *Molecular cell* **67**, 757-769.

Development • Accepted manuscript

Xiao, C., Nitsche, F. and Bazzi, H. (2018). Visualizing the Node and Notochordal Plate In Gastrulating Mouse Embryos Using Scanning Electron Microscopy and Whole Mount Immunofluorescence. *Journal of visualized experiments* **6**, e58321.

Y., K. and Katoh, M. (2005). Comparative genomics on Vangl1 and Vangl2 genes. *International journal of oncology* **26**, 1435-1440.

Yang, Y. and Mlodzik, M. (2015). Wnt-Frizzled/planar cell polarity signaling: cellular orientation by facing the wind (Wnt). *Annual review of cell and developmental biology* **31**, 623-646.

Development • Accepted manuscript

Figures

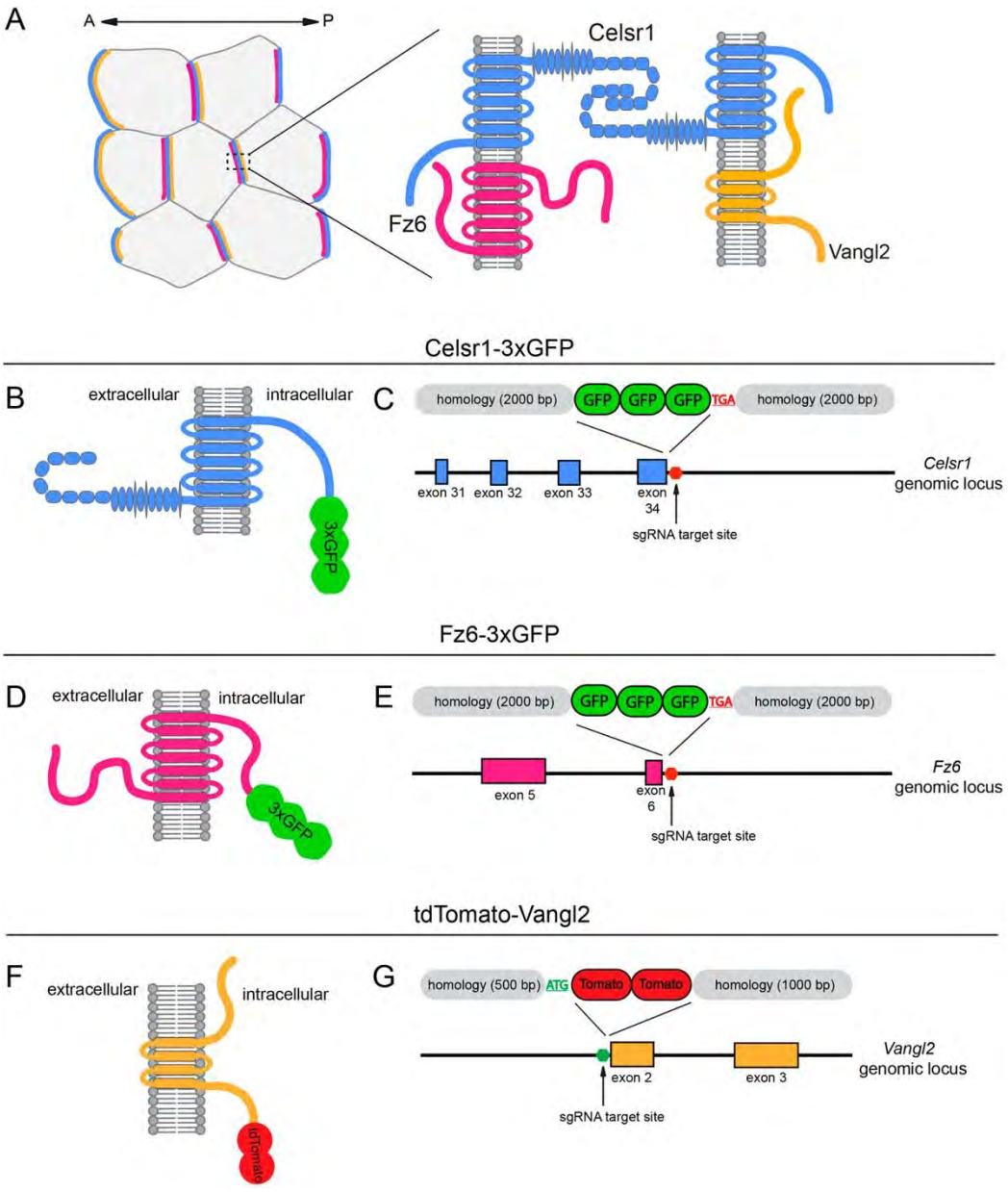

Figure 1. Strategy for endogenously tagging Celsr1, Fz6 and Vangl2. (A) Schematic of the proposed localization of the core transmembrane PCP proteins at the cellular and junctional level. **(B, D, F)** Diagram of Celsr1-3xGFP (B), Fz6-3xGFP (D), and tdTomato-Vangl2 (F) fusion proteins illustrating domain structure and the position of insertion. **(C, E)** Targeting arm design

Development • Accepted manuscript

for the C-terminal Celsr1-3xGFP (C) and Fz6-3xGFP (E) insertion. The *Celsr1* and *Fz6* stop codon targeted by the sgRNA and the C-terminal exons of the *Celsr1* (blue) and *Fz6* (magenta) genomic region are shown. **(G)** Targeting arm design for N-terminal fusion of tdTomato-Vangl2. The *Vangl2* start codon targeted by the sgRNA and the N-terminal exons (orange) of the *Vangl2* genomic region are shown.

Development • Accepted manuscript

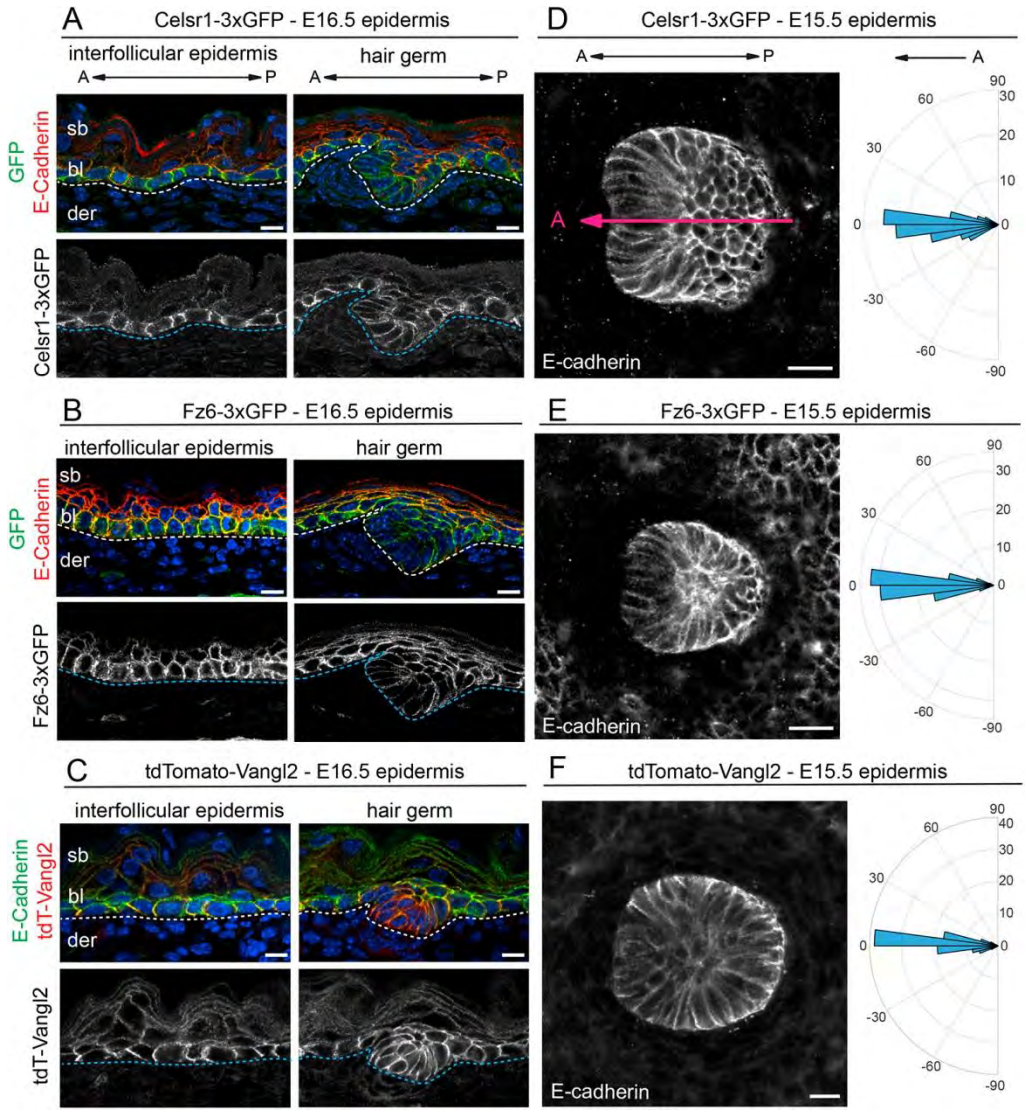

Figure 2. Expression and function of Celsr1-3xGFP, Fz6-3xGFP, and tdTomato-Vangl2 in the embryonic skin. (A-C) Expression and localization of PCP fusion proteins in the interfollicular epidermis (IFE) and developing hair follicles (HF) in E16.5 homozygous embryos. Sagittal cryosections were labeled with E-Cadherin and Hoechst to mark nuclei (blue). Scale bar, 10 μm. **(A)** Celsr1-3xGFP (green), E-cadherin (red). **(B)** Fz6-3xGFP (green), E-cadherin (red). **(C)** tdTomato-Vangl2 (red), E-cadherin (green). Dotted lines indicate position of the epidermal-dermal boundary. sb=suprabasal layer, bl=basal layer, der=dermis. Note that Celsr1-3xGFP, Fz6-3xGFP and tdTomato-Vangl2 are expressed primarily in the basal layer. **(D-F)** HF orientations at E15.5. Planar views of single HFs of flat mount epidermis with E-cadherin are shown. Quantification of HF alignment is shown in circular histograms. Anterior is to the left (at 0º). Vectors point toward the anterior, growing end of HFs. **(D)** Celsr1-3xGFP, n = 184, 3

Development • Accepted manuscript

embryos. Magenta line overlaid on the HF indicates orientation, where the anterior is marked by low E-cadherin expression. **(E)** Fz6-3xGFP homozygous, n = 361, 3 embryos. **(F)** tdTomato-Vangl2 homozygotes with a curly tail and closed neural tube phenotype (CNT), n = 434, 3 embryos. Note that in all three homozygous lines, HFs point anteriorly and align along the A-P axis similar to their orientations in wild type epidermis (Supplemental Figure 1).

Development • Accepted manuscript

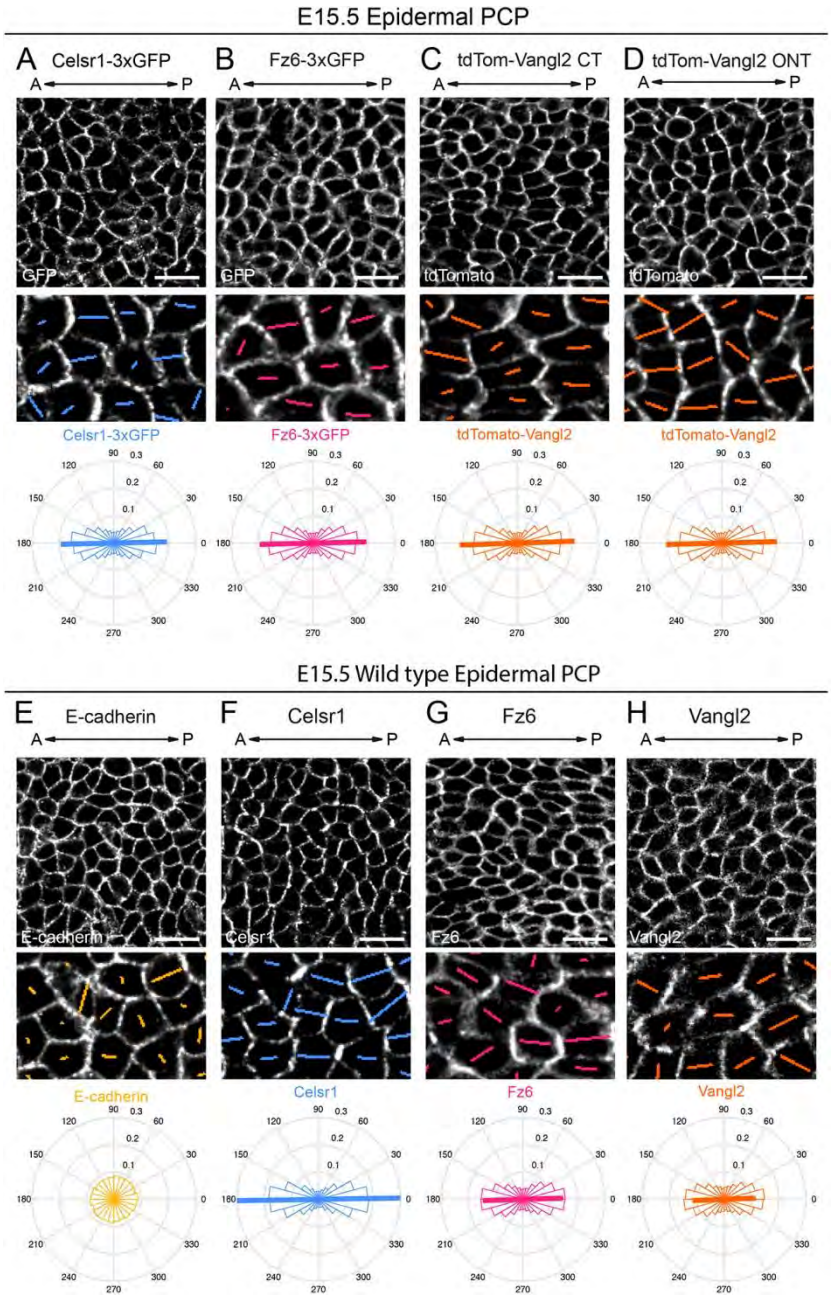

Figure 3. Planar polarized distribution of Celsr1-3xGFP, Fz6-3xGFP, and tdTomato-Vangl2 in the epidermis. (A-H) Representative planar views of the basal layer of the IFE in E15.5 epidermis showing fluorescently-tagged PCP protein distributions in homozygous embryos (A-D) and Celsr1, Fz6, Vangl2, and E-cadherin localization in wild-type epidermis as detected by immunofluorescence against the endogenous, untagged proteins (E-H). Anterior is to the left. Scale bar, 20 μm. Magnified areas below are overlaid with colored lines representing the axis (line angle) and magnitude (line length) of polarity. Quantification of polarity distributions are

Development • Accepted manuscript

displayed below on circular histograms. **(A)** Celsr1-3xGFP, n = 13,605 basal cells, 3 embryos. **(B)** Fz6-3xGFP, n = 18,665 basal cells, 3 embryos. **(C)** tdTomato-Vangl2 in embryos displaying a CNT phenotype (CNT), n = 10,775 basal cells, 3 embryos. **(D)** tdTomato-Vangl2 in embryos displaying and open neural tube (ONT) phenotype, n = 9,884 basal cells, 3 embryos. **(E)** E-cadherin, n = 12,669 basal cells, 3 embryos. Note that compared to endogenous and tagged PCP proteins, E-Cadherin is uniformly distributed at cell junctions. **(F)** Celsr1 distribution, n = 12,669 basal cells, 3 embryos. **(G)** Fz6 distribution, n = 8,162 basal cells, 3 embryos. **(H)** Vangl2 distribution, n = 9,300 basal cells, 3 embryos.

Development • Accepted manuscript

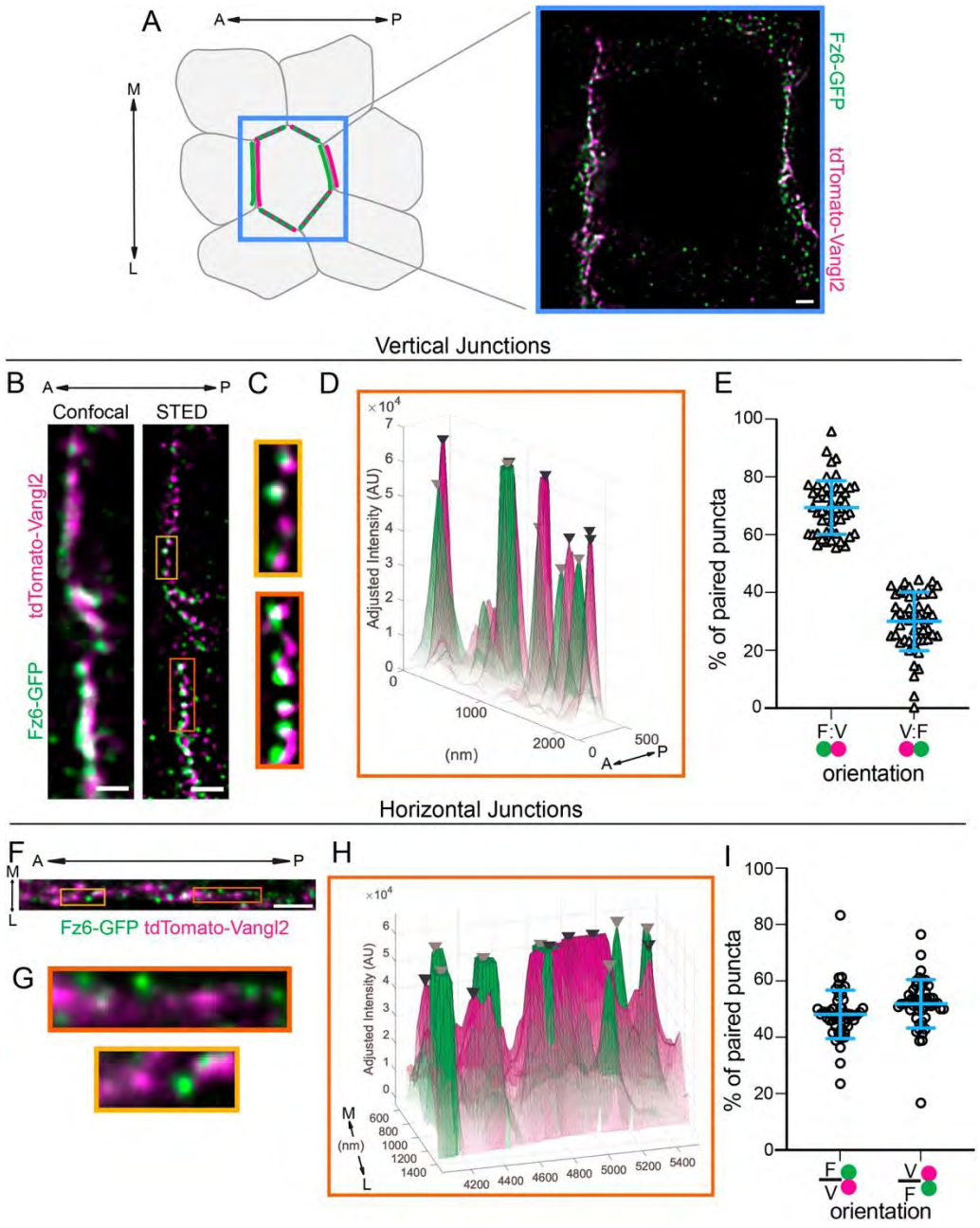

Figure 4. Super resolution (STED) imaging of Fz6-3xGFP and tdTomato-Vangl2 resolves their asymmetric localization. Whole mount E15.5 Fz6-3xGFP/Fz6-3xGFP; tdTomato-Vangl2/+ skins labeled for GFP and tdTomato and imaged using simulated emission depletion microscopy (STED). Anterior is oriented to the left. **(A)** Schematic of PCP localization in basal epidermal cells. Anterior-posterior (vertical) and mediolateral (horizontal) junctions of a single cell are highlighted. STED image of a full cell with Fz6-3xGFP (green) and tdTomato-Vangl2 (magenta). Note that horizontal junctions appear less bright and punctate than vertical junctions.

Development • Accepted manuscript

Scale bar, 1 μm. **(B-I)** STED imaging and analysis of vertical (B-E) and horizontal (F-I) junctions. **(B, F)** Representative planar view of Fz6-3xGFP (green) and tdTomato-Vangl2 (magenta) localization at a vertical junction imaged using standard confocal imaging (left) and STED (right) (B) and at a horizontal junction (F). Scale bar, 1 μm. **(C, G)** Magnified regions of the junction corresponding to the boxed areas in (B) and (F). **(D, H)** Corresponding surface plots of GFP and tdTomato fluorescence intensity along the junction of the magnified region outlined in orange in (B) and in orange in (F). Arrowheads mark peaks of fluorescence intensity. Opacity of the plot corresponds to pixel intensity, with low opacity indicating low pixel intensity and high opacity indicating high pixel intensity. Note in horizontal junctions (H) that the non-peak signal is more diffuse with higher opacity compared to vertical junctions. **(E)** Quantification of the orientation of puncta pairs in vertical junctions. The percent of puncta pairs along a junction in the F:V orientation (where Fz6-3xGFP localizes to the anterior of each puncta pair) versus the V:F orientation, n = 50 junctions, 3 embryos. Blue bar overlay indicates the mean ± s.d across all junctions. **(I)** Quantification of the orientation of puncta pairs in horizontal junctions. The percent of puncta pairs along a junction in the F/V orientation (where Fz6-3xGFP localizes to the medial side of the pair) versus V/F orientation, n = 51 junctions, 3 embryos. Blue bar overlay indicates the mean ± s.d across all junctions.

Development • Accepted manuscript

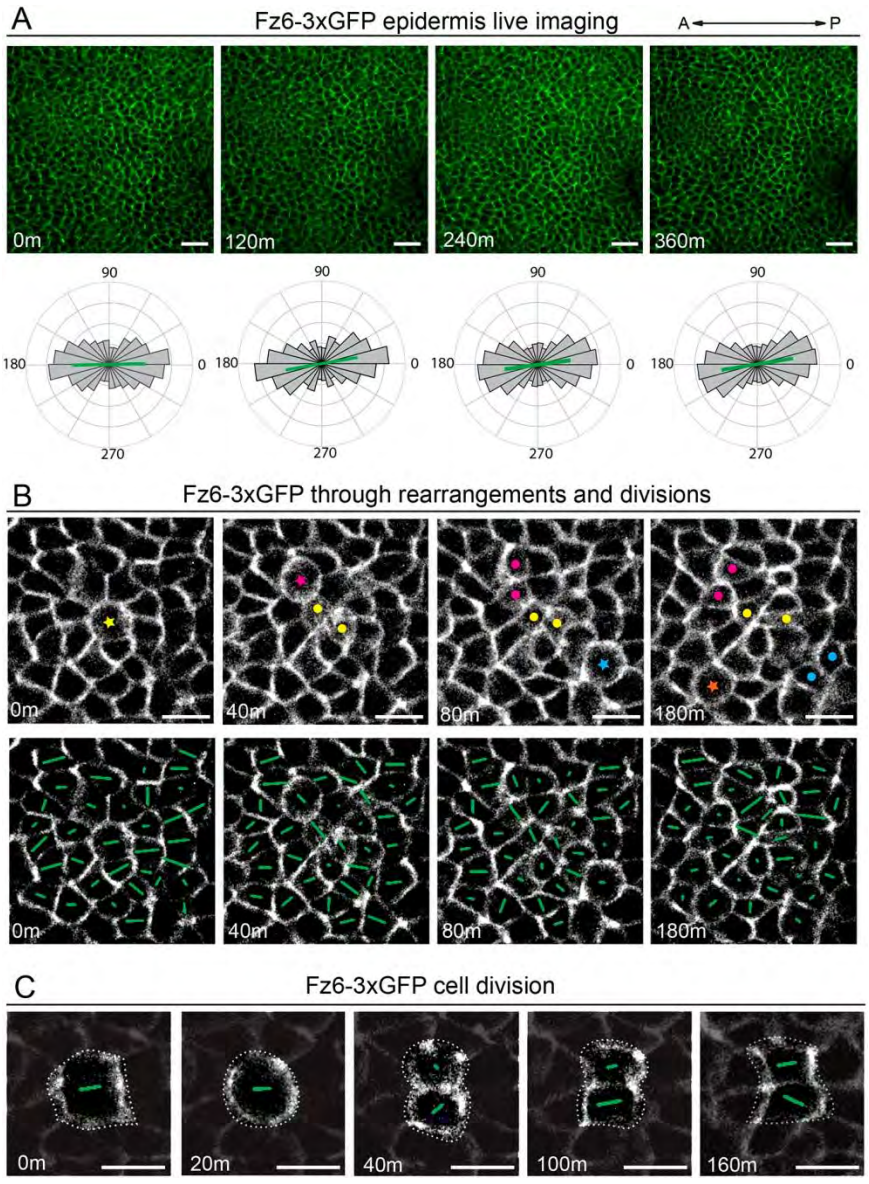

Figure 5. Fz6-3xGFP localization is highly dynamic during cell rearrangements and divisions yet the global axis of asymmetry is maintained. (A) Still frames from live imaging of Fz6-3xGFP homozygous E15.5 skin explants at 0,2,4, and 6 hour time points. Circular histograms below show quantification of Fz6-3xGFP polarity across the entire field of view. Note the orientation and magnitude of the polarity is maintained over the time course. Scale bar, 40 μm. **(B)** Still frames of Fz6-3xGFP live imaging during cell divisions and rearrangements. Top panels: a colored dot indicates cells in mitosis and a pair of dots after cytokinesis. Bottom panels: same still frames as above with polarity nematics overlaid. Note that Fz6-3xGFP polarity within individual cells is not fixed through time, rather polarity changes in magnitude and

Development • Accepted manuscript

orientation especially with division. Scale bar, 20 μm. **(C)** Representative example of Fz6-3xGFP during cell division. Polarity nematics are overlaid on the dividing cell (dashed outline), and neighboring cells are darkened to emphasize Fz6-3xGFP in the dividing cell. Note in this example, daughter cells share the same axis of asymmetry as the mother cell's prior to mitosis. Scale bar, 20 μm.

Development • Accepted manuscript

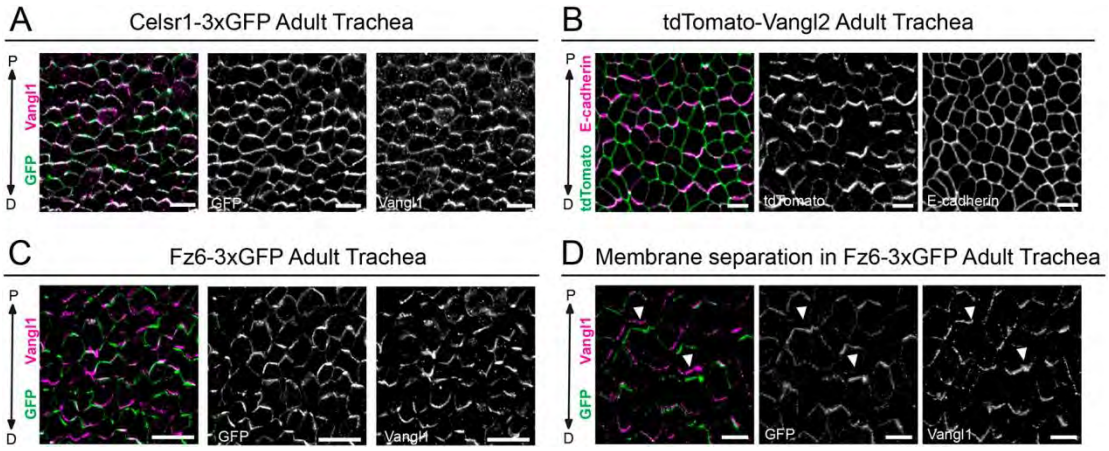

Figure 6. Polarized localization of Celsr1-3xGFP, and mutually exclusive localization of tdTomato-Vangl2 and Fz6-3xGFP to opposite cell edges in the adult trachea. (A-C) Representative planar view of flat-mounted trachea from **(A)** homozygous Celsr1-3xGFP adult labeled with antibodies against GFP (green) and Vangl1 (magenta). Note that Celsr1-3xGFP and Vangl1 are asymmetrically localized at proximal-distal junctions. Proximal is oriented up. Scale bars, 10 μm. **(B)** heterozygous tdTomato-Vangl2 adult labeled with tdTomato (magenta) and E-cadherin (green). tdTomato-Vangl2 is asymmetrically localized along the P-D axis, whereas E-cadherin is uniform around cell edges. Scale bars, 5 μm. **(C)** Fz6-3xGFP homozygous adult labeled with GFP (green) and Vangl1 (magenta). Fz6-3xGFP and Vangl1 are polarized along the P-D axis. Scale bars, 10 μm. **(D)** Representative image showing mutually exclusive localization of Fz6-3xGFP and Vangl1 localization to opposing sides of P-D junctions in cells where membranes have separated due to methanol fixation (arrows indicate areas showing opposing localization across cell junctions). Scale bars, 10 μm.

Development • Accepted manuscript

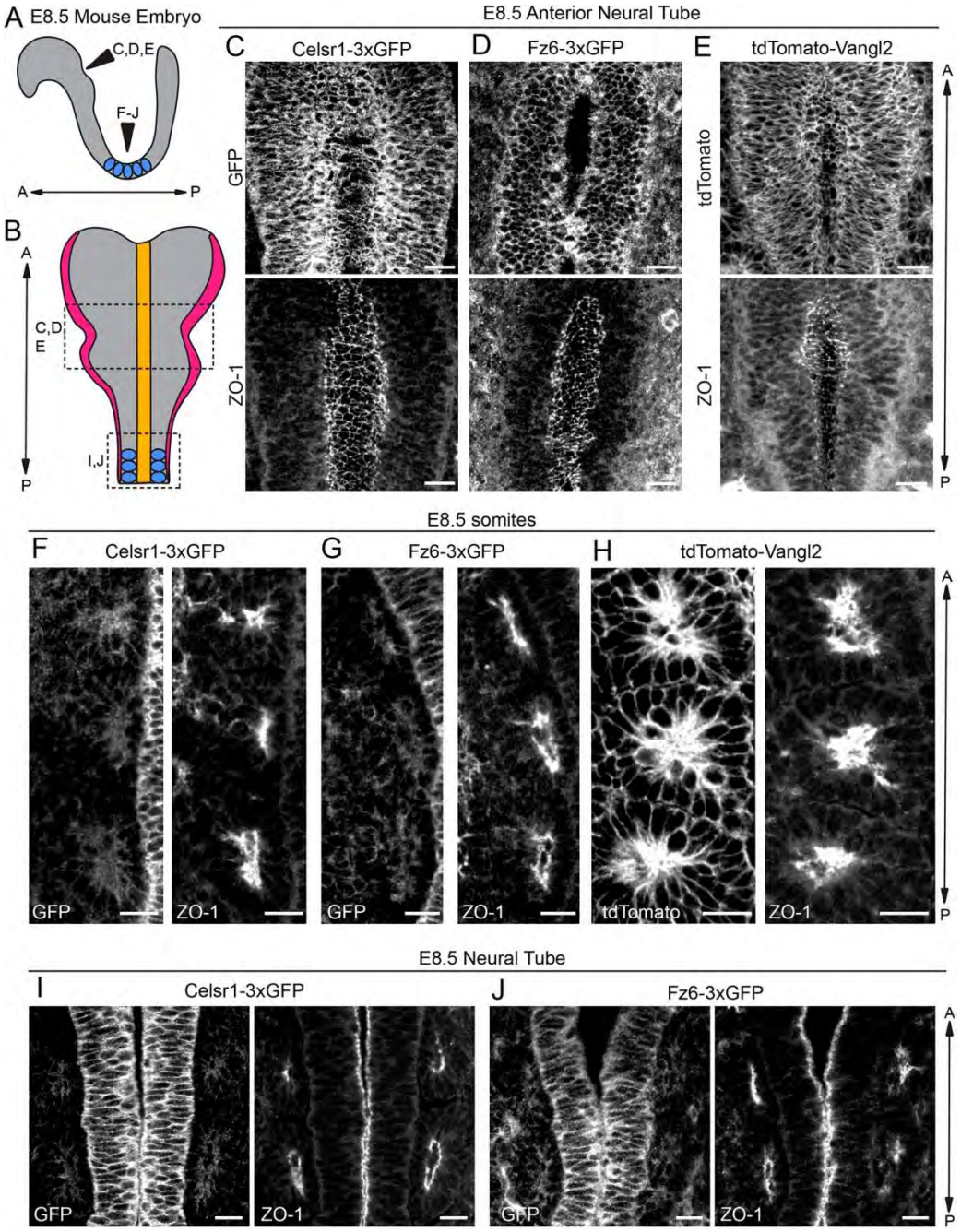

Figure 7. Celsr1-3xGFP, Fz6-3xGFP and tdTomato-Vangl2 in the early embryo: neural tube and somites. (A) Schematic of lateral view of E8.5 embryo showing positions of neural tube imaged in C-J and somites (blue). **(B)** Schematic of dorsal view of E8.5 embryo showing neural folds and somites. Adapted from (Brooks et al., 2020). **(C-E)** Representative images of endogenously-tagged PCP protein localization in the rostral neural tube of E8.5 homozygous embryos labeled with ZO-1 to mark the apical positions of neural epithelial cells. Maximum

Development • Accepted manuscript

intensity projections of 5-8 μm are shown. Scale bars, 20 μm. **(C)** Celsr1-3xGFP (left), ZO-1 (right). **(D)** Fz6-3xGFP (left), ZO-1 (right). Note a single plane was chosen for the Fz6-3xGFP channel to more clearly display its localization. **(E)** tdTomato-Vangl2 (left), ZO-1 (right). **(F-H)** Representative images showing endogenously-tagged PCP protein localization in the somites of E8.5 homozygous embryos labeled with ZO-1. Three somites from one side of the midline are shown. Scale bars, 10 μm. **(F)** Celsr1-3xGFP (left) and ZO-1 (right). **(G)** Fz6-3xGFP (left) and ZO-1 (right). **(H)** tdTomato-Vangl2 (left) and ZO-1 (right). Note strong expression of tdTomato-Vangl2 in somites compared to Celsr1-3xGFP and Fz6-3xGFP. **(I-J)** Representative images of Celsr1-3xGFP and Fz6-3xGFP localization at a more caudal position of the neural tube that has already closed at E8.5. Scale bars, 10 μm. **(I)** Celsr1-3xGFP (left) and ZO-1 (right). **(J)** Fz6-3xGFP (left) and ZO-1 (right). Scale bars, 20 μm.

Development • Accepted manuscript

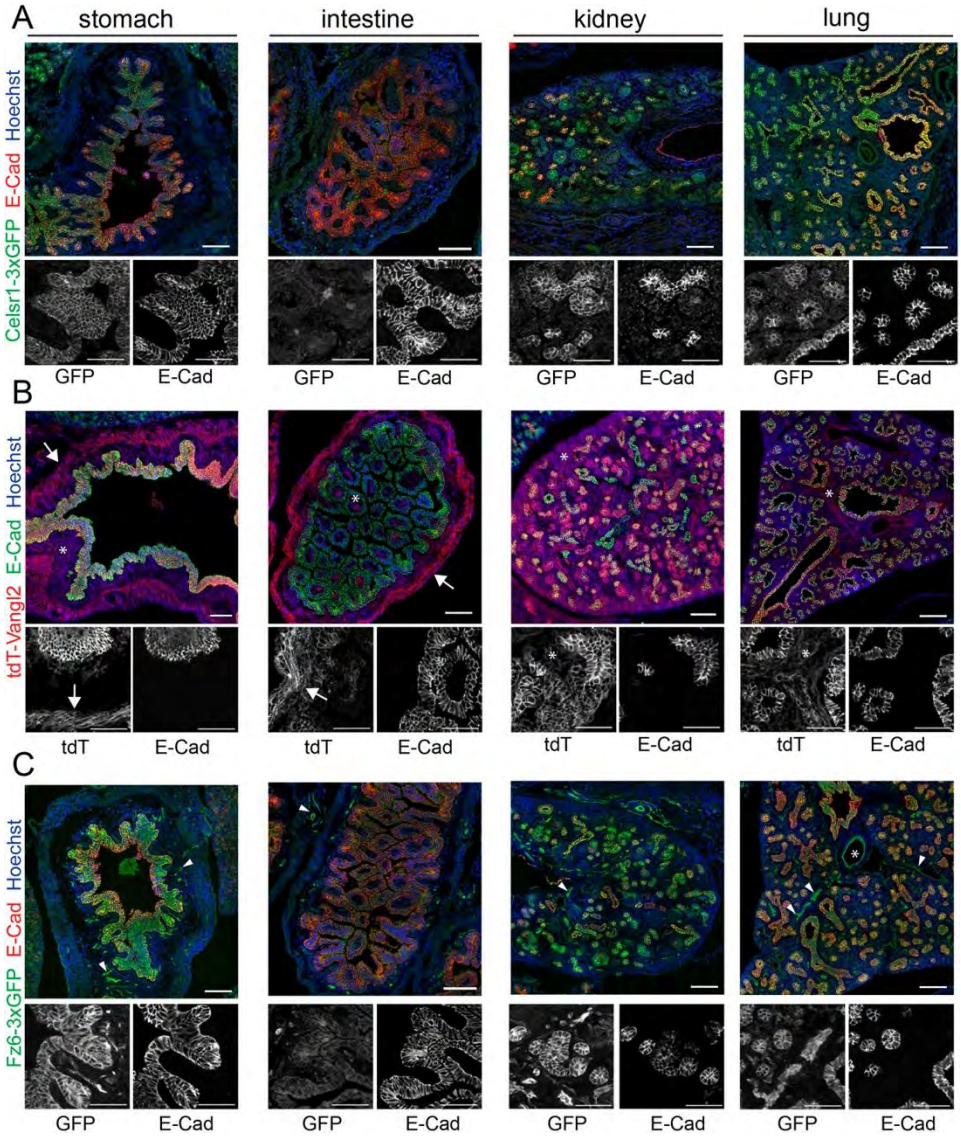

Figure 8. Celsr1-3xGFP, Fz6-3xGFP and tdTomato-Vangl2 expression and localization across embryonic organs. Sagittal sections from Celsr1-3xGFP, tdTomato-Vangl2 and Fz6-3xGFP embryos at E16.5 labeled with E-Cadherin to mark epithelia and Hoechst (blue) to mark nuclei. **(A-C)** Composite images of E16.5 sagittal sections showing Celsr1-3xGFP (A, green), tdTomato-Vangl2 (B, red) and Fz6-3xGFP (C, green) expression in the stomach, intestine, kidney and lungs. Below each merged image are zoomed-in regions of individual channels in greyscale. **(A)** Celsr1-3xGFP (green), E-Cadherin (red), Hoechst. **(B)** tdTomato-Vangl2 (red); E-Cadherin (green), Hoechst. Arrows indicate expression in smooth muscle, asterisks denote expression in stromal cells. **(C)** Fz6-3xGFP (green), E-Cadherin (red), Hoechst. Arrowheads points to expression in vasculature. Asterisk marks the lumen of a blood vessel in the lung. Scale bars, 100 μm for merged images, and 50 μm for greyscale images.

Development • Accepted manuscript

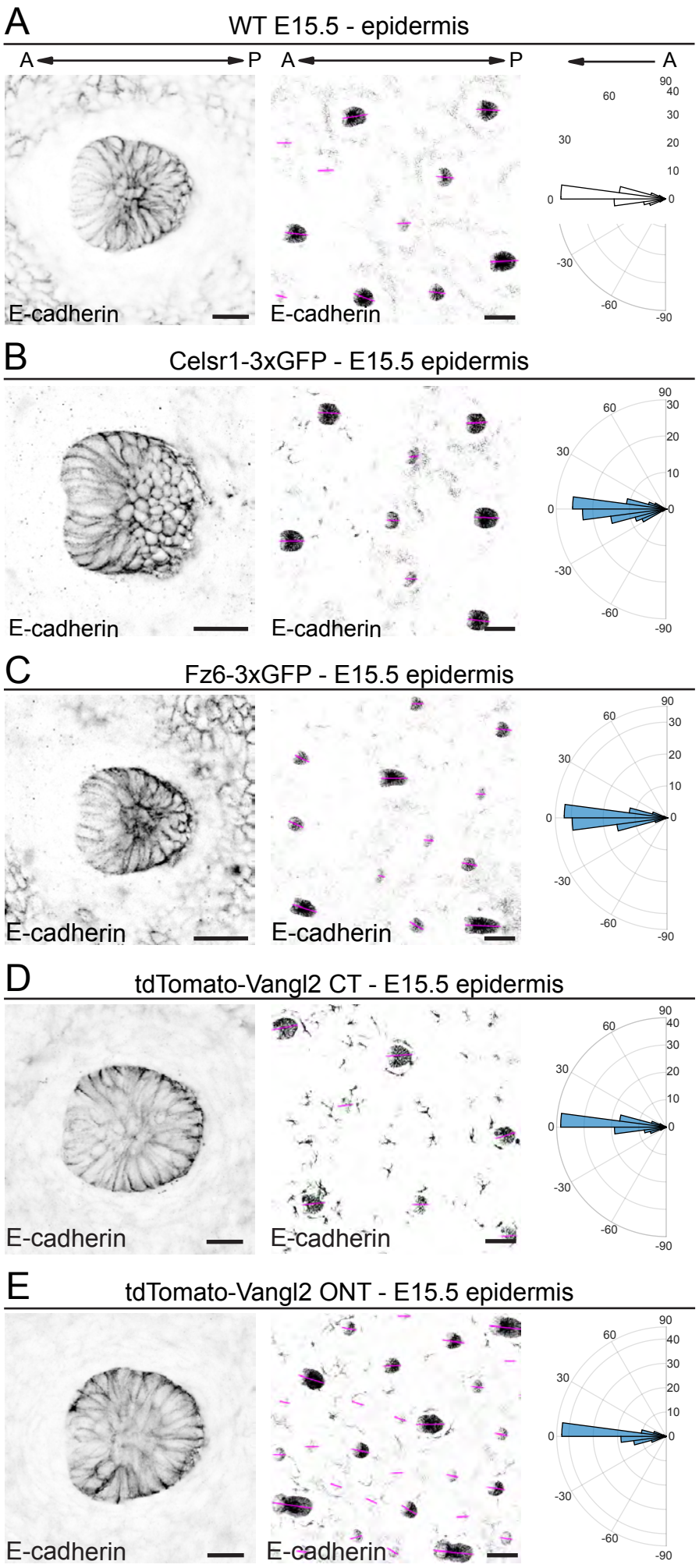

Fig. S1. Analysis of hair follicle orientation in Celsr1-3xGFP, Fz6-3xGFP, and tdTomato-Vangl2 homozygous embryos. (**A-E)** Hair follicle (HF) orientations at E15.5. Planar views of single follicles and larger areas of flat mount epidermis labeled with E-Cadherin are shown. Magenta lines overlaid developing HFs denote their orientation. Scale bar, 100 μm. Quantification of hair follicle alignment is shown in circular histograms. Anterior is to the left (at 0º). Vectors point toward the anterior, growing end of HFs. **(A)** wild type, n = 987 from 4 embryos. **(B)** Celsr1-3xGFP, n = 184 from 3 embryos. **(C)** Fz6-3xGFP homozygous, n = 361 from 3 embryos. **(D)** tdTomato-Vangl2 homozygotes with a curly tail and closed neural tube phenotype (CNT), n = 434 from 3 embryos. **(E)** tdTomato-Vangl2 homozygotes with an open neural tube (ONT) phenotype, n = 601 from 3 embryos. Note that in tdTomato-Vangl2 embryos of both phenotypes, hair follicles point anteriorly and align along the A-P axis similar to their orientations in wild type epidermis.

Development • Supplementary information

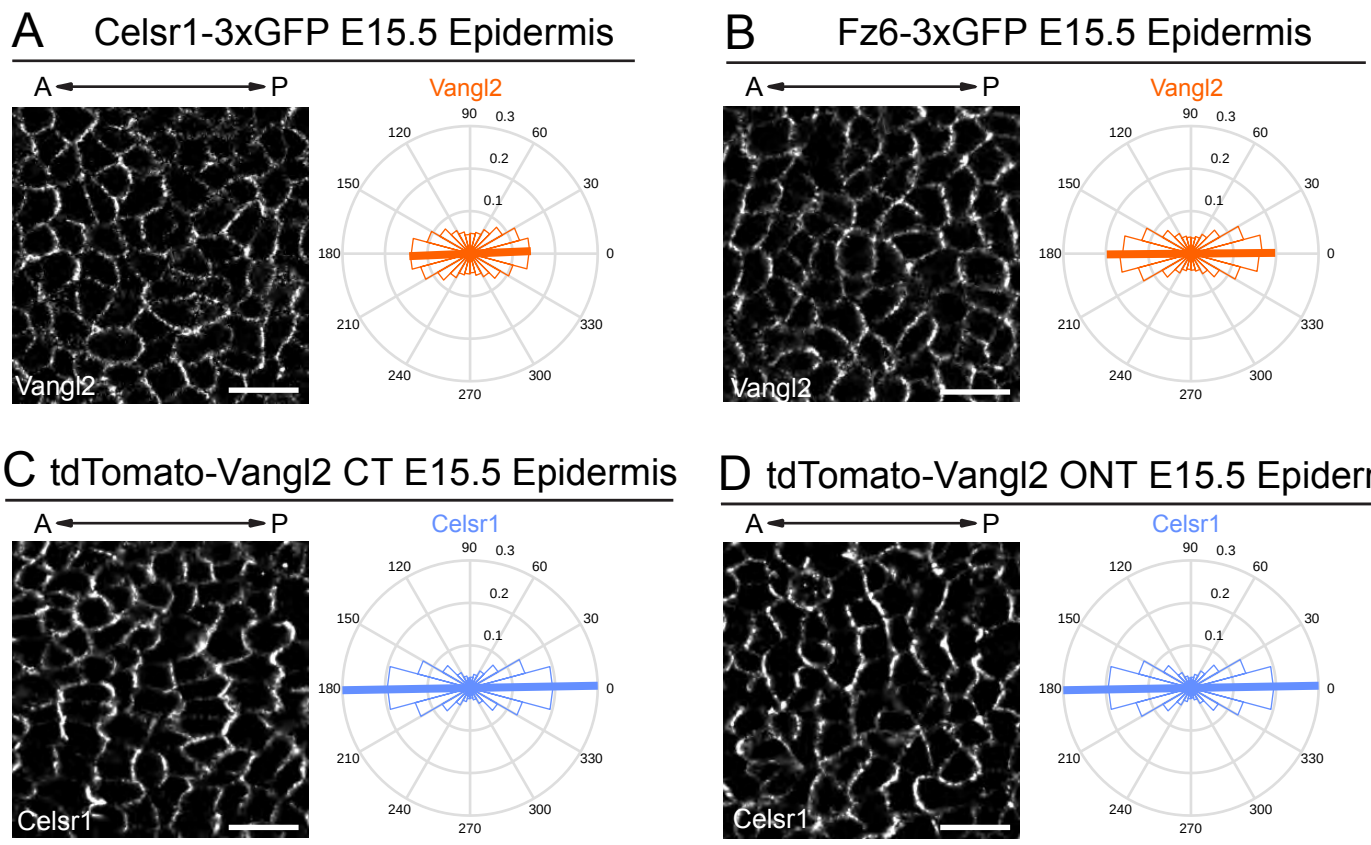

Fig. S2. Comparison of PCP protein asymmetry in Celsr1-3xGFP, Fz6-3xGFP, and tdTomato-Vangl2. **(A-B)** Representative planar views of Vangl2 immunofluorescence in the basal layer of the IFE from Celsr1-3xGFP and Fz6-3xGFP homozygous embryos at E15.5. Quantification of Vangl2 polarity is shown below on circular histograms. **(A)** Vangl2 in Celsr1-3xGFP epidermis, n = 13,605 basal cells from 3 embryos. **(B)** Vangl2 in Fz6-3xGFP epidermis, n = 9,778 from 3 embryos. **(C-D)** Representative planar views of Celsr1 immunofluorescence in the basal layer of the IFE from tdTomato-Vangl2 homozygous embryos at E15.5. Circular histograms below display quantification of Celsr1 polarity **(C)** Celsr1 localization in tdTomato-Vangl2 homozygotes with the curly tail and closed neural tube phenotype (CNT), n = 10,775 basal cells from 3 embryos. **(D)** Celsr1 localization in tdTomato-Vangl2 homozygotes with open neural tube (ONT) phenotypes, n = 9,884 basal cells from 3 embryos. Scale bars, 20 μm.

Development • Supplementary information

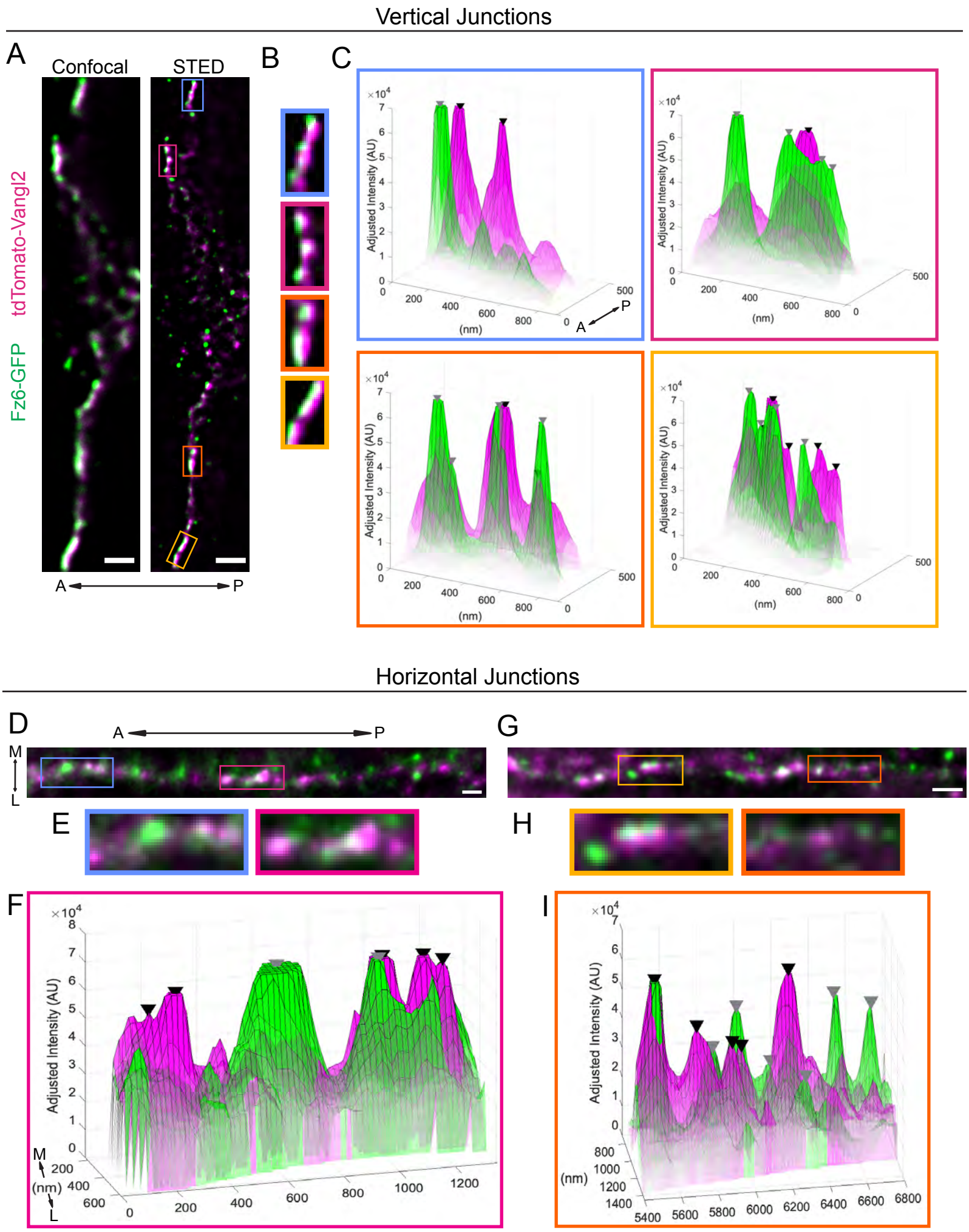

Development • Supplementary information

Fig. S3. Super resolution (STED) imaging of Fz6-3xGFP and tdTomato-Vangl2 resolves their localization at vertical and horizontal junctions. (A) Additional representative examples of Fz6-3xGFP and tdTomato-Vangl2 localization across two vertical junctions imaged using standard confocal imaging and STED. Scale bar, 1 μm. **(B)** Magnified regions of the junction corresponding to the boxed areas in (A). **(C)** Corresponding surface plots of GFP and tdTomato fluorescence intensity along the junction of the magnified regions in (B). Arrowheads mark peaks of fluorescence intensity. Opacity of the plot corresponds to pixel intensity, with low opacity indicating low pixel intensity and high opacity indicating high pixel intensity. **(D, G)** Additional representative examples of Fz6-3xGFP and tdTomato-Vangl2 localization across two horizontal junctions imaged using STED. Scale bar, 500 nm. **(E, H)** Magnified regions of the junction corresponding to the boxed areas in (D, G). **(F, I)** Corresponding surface plots of GFP and tdTomato fluorescence intensity along the junction of the magnified region outline in magenta in (D, E) and the region outlined in orange in (G, H). Arrowheads mark peaks of fluorescence intensity. Opacity of the plot corresponds to pixel intensity, with low opacity indicating low pixel intensity and high opacity indicating high pixel intensity.

Development • Supplementary information

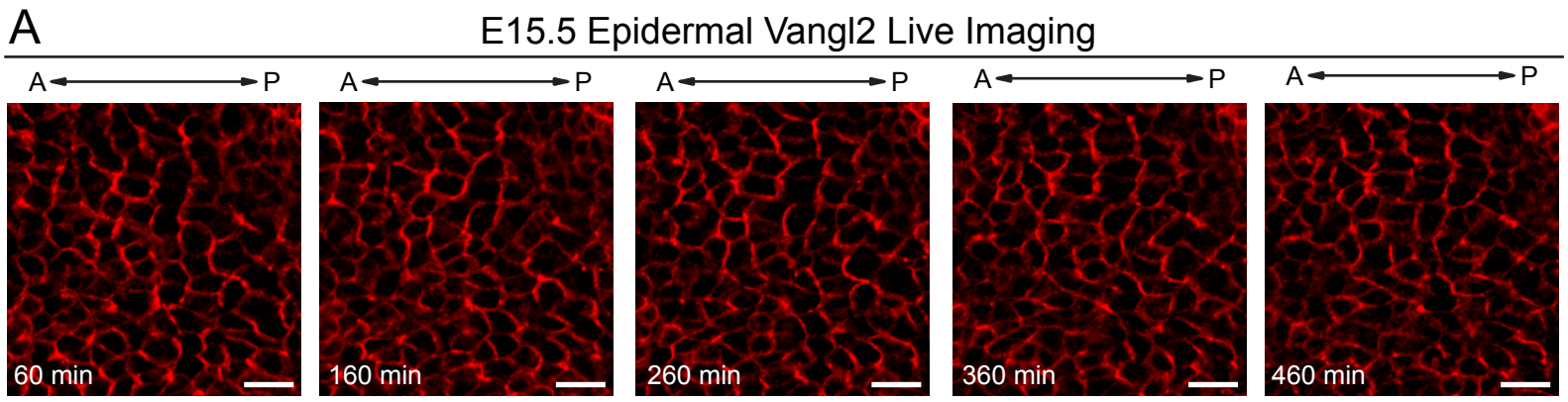

Fig. S4. tdTomato-Vangl2 live imaging. Still frames from live imaging of tdTomato-Vangl2 homozygous E15.5 skin explants at indicated time points. Scale bar, 40 μm.

Development • Supplementary information

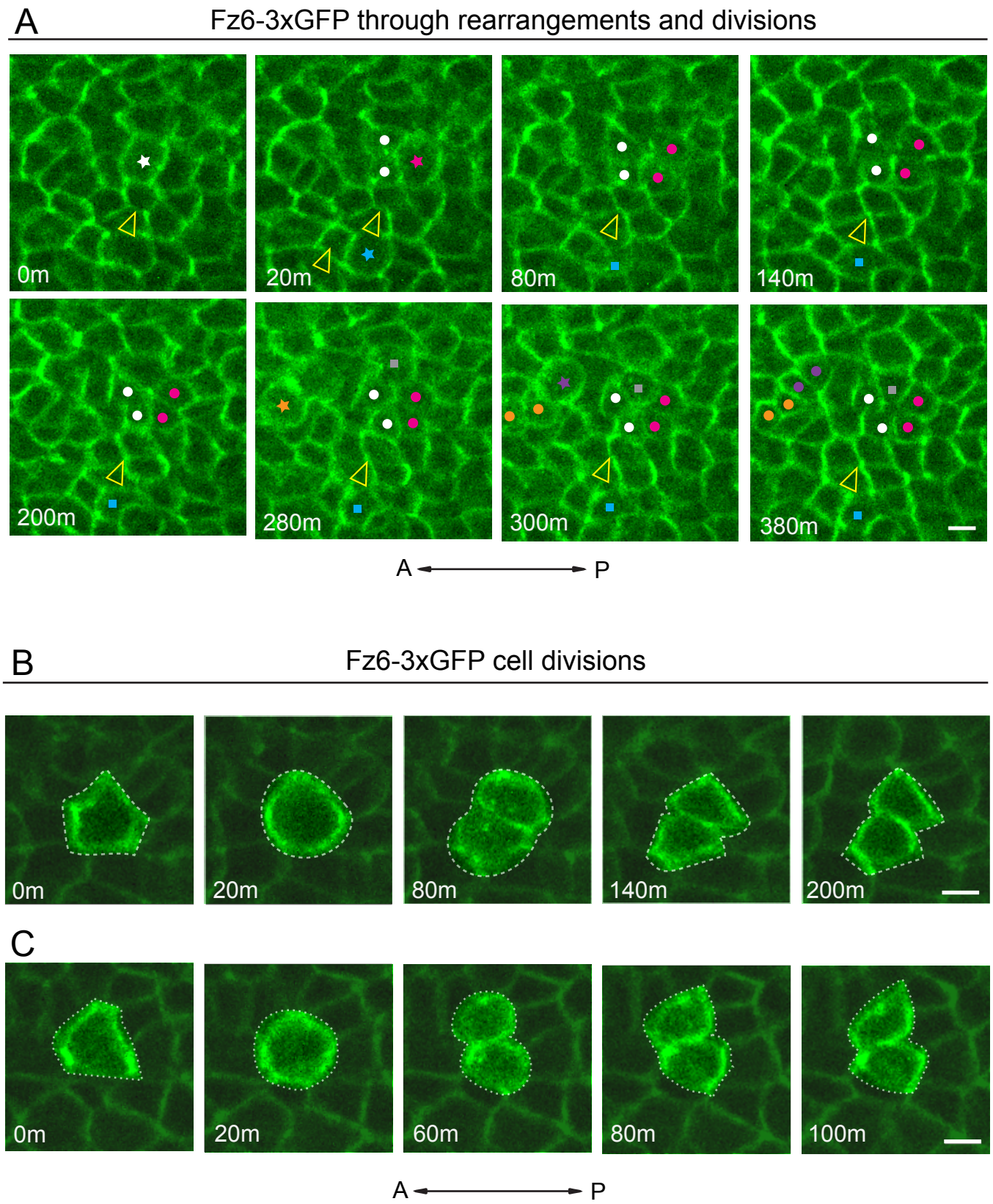

Fig. S5. Live imaging of Fz6-3xGFP through cell rearrangements and divisions. Additional examples of Fz6-3xGFP dynamics through time. **(A)** Still frames of Fz6-3xGFP live images during cell divisions and rearrangements. Each division is indicated by a colored star in mitosis and a pair of dots after cytokinesis. Yellow arrowhead marks a junctional remodeling event. Note the horizontal junction at 0m shrinks to a 4-cell vertex at 140m. **(B-C)** Representative examples of Fz6-3xGFP during cell division (dashed outlines). Neighboring cells are darkened to emphasize Fz6-3xGFP in the dividing cell. Note in these examples, the polarity of daughter cells does not align identically with the polarity of the mother cell prior to mitosis.

Development • Supplementary information

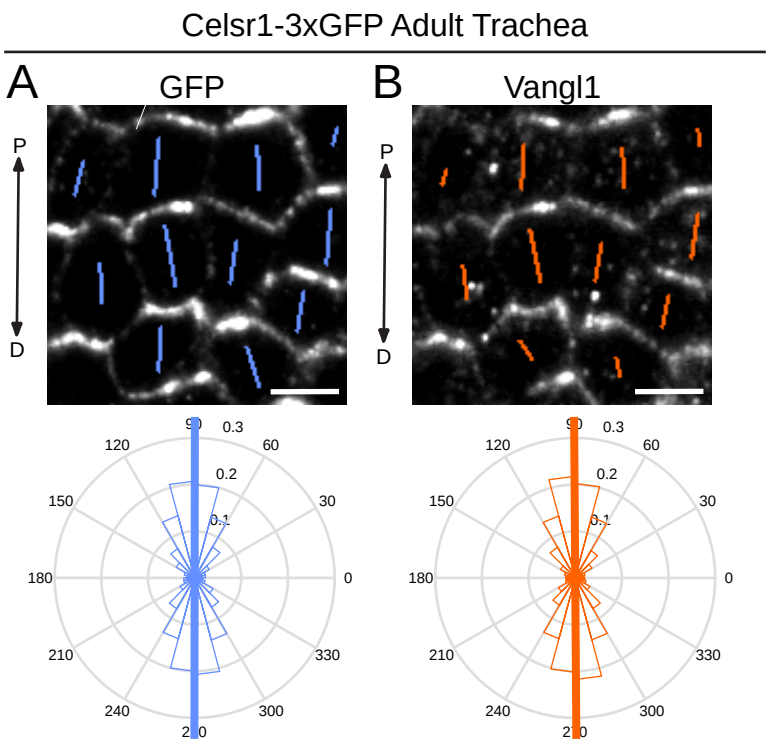

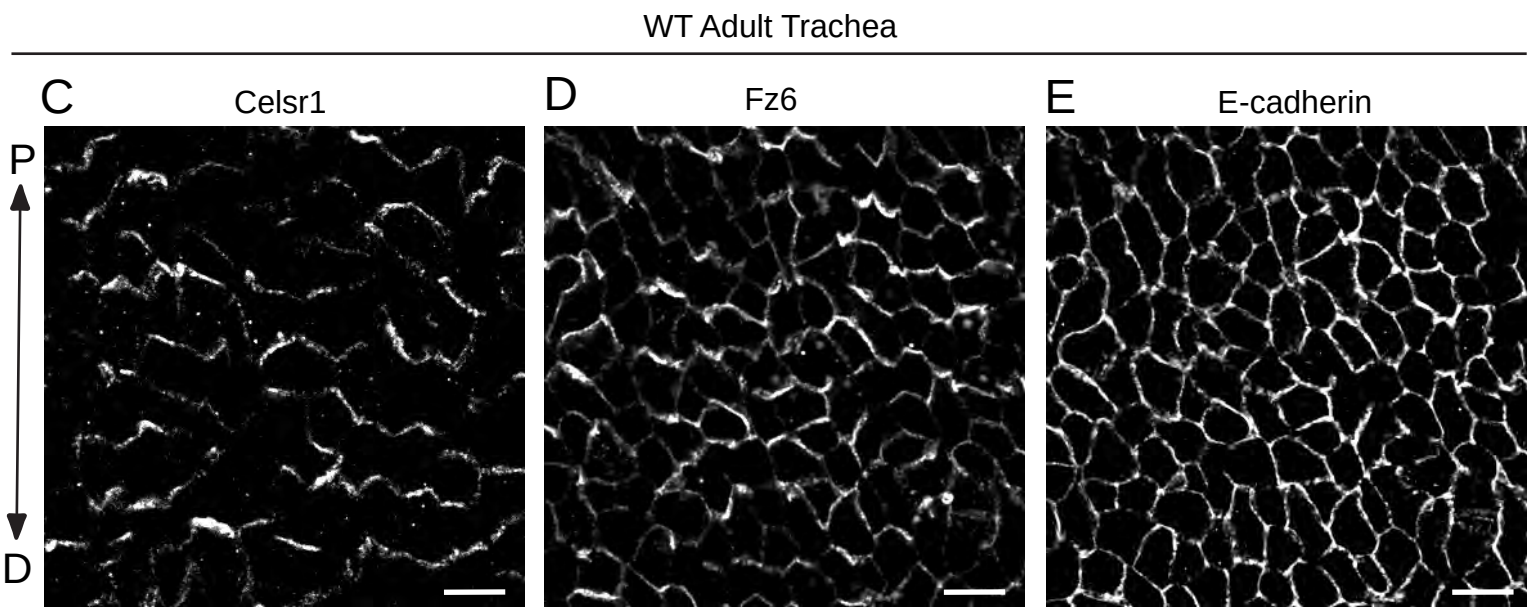

Fig. S6. Celsr1-3xGFP polarity quantification in adult trachea and comparison in wild-type trachea. Representative immunofluorescence images of Celsr1-3xGFP **(A)** and Vangl1 **(B)** in adult trachea. Lines represent the magnitude (line length) and axis (line angle) of polarity. Circular histograms below show the distribution of Celsr1-3xGFP polarity (A) and Vangl1 (B) in the adult trachea, n = 3,228 cells from 3 adult tracheas. Scale bars, 5 μm. **(C-E)** Representative immunofluorescence images of Celsr1 (C), Fz6 (D) and E-cadherin (E) in wild-type adult trachea. Scale bars, 10 μm.

Development • Supplementary information

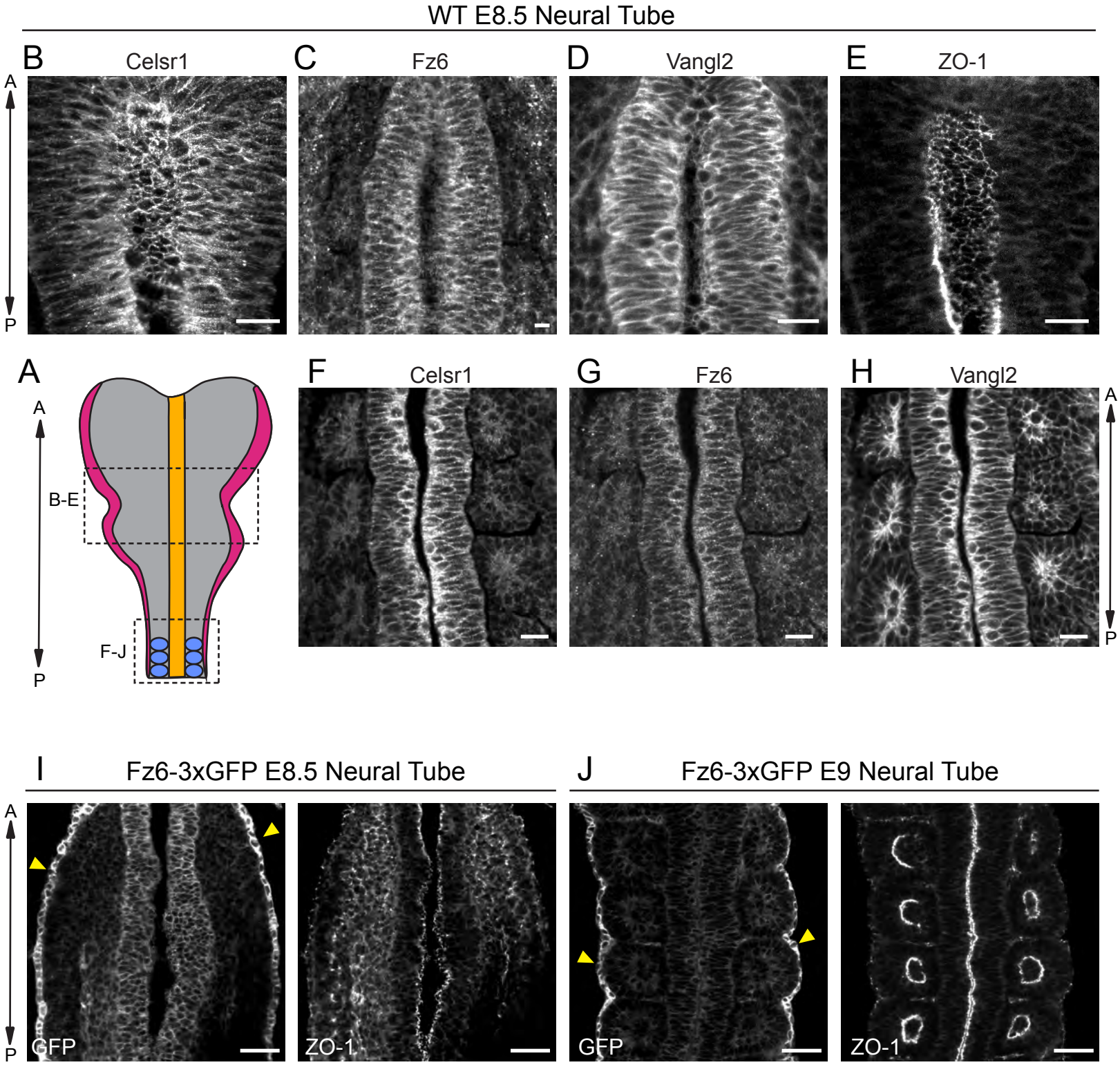

Development • Supplementary information

Fig. S7. Expression of PCP proteins in wild-type E8.5 embryos and Fz6-3xGFP expression in the E8.5 and E9.5 surface ectoderm and neural tube. (A) Schematic of dorsal view of E8.5 embryo showing neural folds and somites. Schematics adapted from (Brooks et al., 2020). **(B-E)** Representative images of PCP protein localization in the rostral neural tube of E8.5 wild-type embryos as detected by immunofluorescence of endogenous proteins. Maximum intensity projections of 3-7 μm are shown. Scale bars, 20 μm. **(B)** Celsr1 **(C)** Fz6 **(D)** Vangl2 **(E)** ZO-1 to mark the apical positions of neural epithelial cells. **(F-G)** Representative images showing PCP protein localization in the neural tube and somites at more caudal positions of E8.5 wild-type embryos. Scale bars, 20 μm. **(F)** Celsr1 **(G)** Fz6 **(H)** Vangl2. **(I)** Representative image of Fz6-3xGFP and ZO-1 expression in the midline and surface ectoderm of Fz6-3xGFP homozygous E8.5 embryos. Scale bars, 10 μm. **(J)** Representative image of Fz6-3xGFP and ZO-1 in the midline and somites of Fz6-3xGFP homozygous E9 embryos in which the neural tube is fully closed. Note high expression of Fz6-3xGFP in the surface ectoderm (yellow arrowheads) compared to the neural epithelium and somites. Scale bars, 40 μm.

Development • Supplementary information

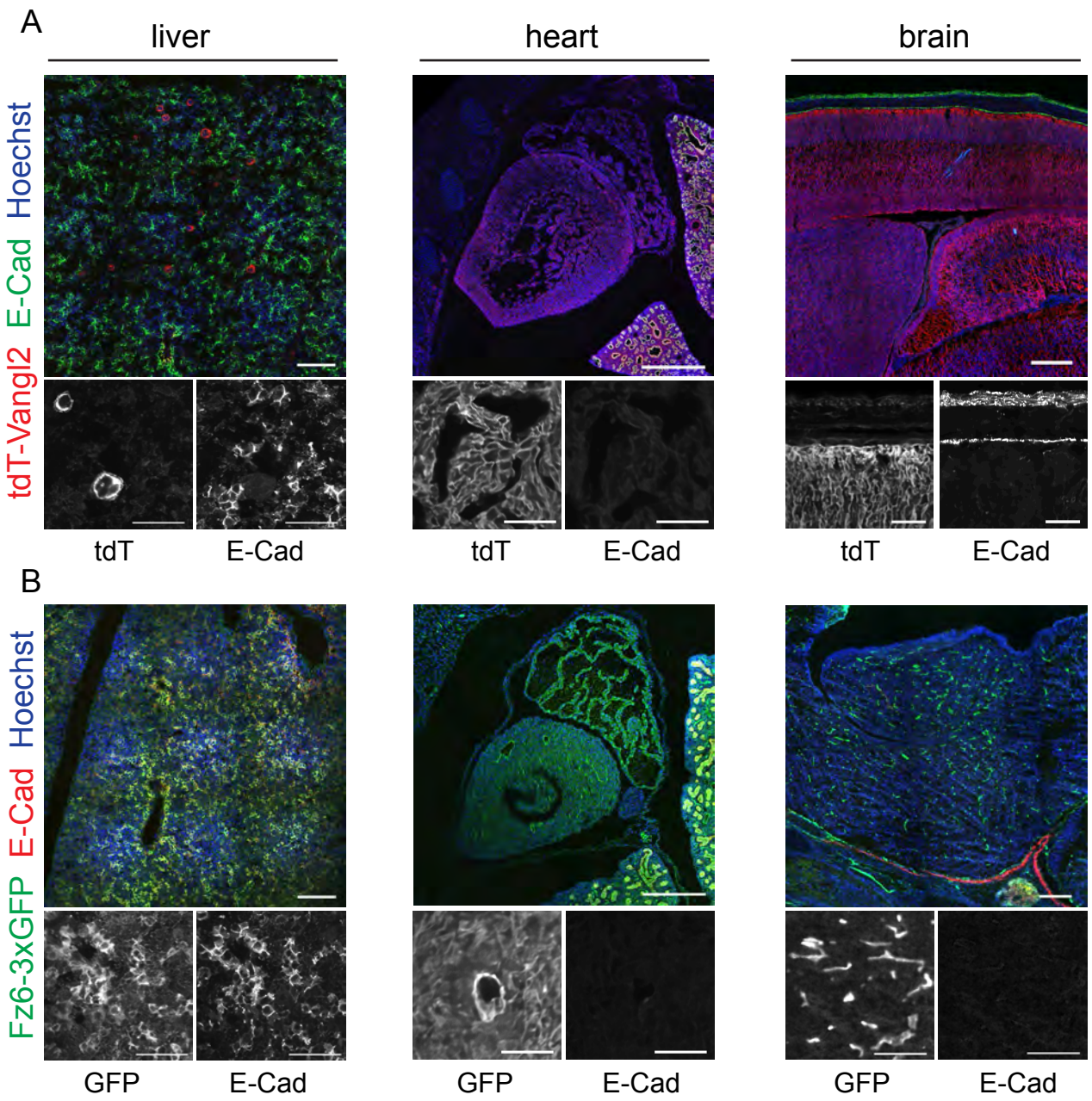

Fig. S8. Fz6-3xGFP and tdTomato-Vangl2 expression in the liver, heart and brain. Sagittal sections from tdTomato-Vangl2 and Fz6-3xGFP embryos at E16.5 labeled with E-Cadherin and Hoechst. **(A-B)** Composite images of E16.5 sagittal sections showing tdTomato-Vangl2 (A, red) and Fz6-3xGFP (B, green) expression in the liver, heart, and brain as indicated. Below each merged image, zoomed-in regions of individual channels in greyscale are shown. **(A)** tdTomato-Vangl2 (red); E-Cadherin (green), Hoechst (blue). tdTomato-Vangl2 is expressed is sparsely labeled cells scattered throughout the liver, broadly throughout the heart including cardiac muscle, and in neurons in the brain. **(B)** Fz6-3xGFP (green), E-Cadherin (red), Hoechst (blue). Note Fz6-3xGFP is expressed in liver epithelium as well as the vasculature in all three tissues. Scale bars, 100 μm for merged images, 500 μm for composite images of the heart, and 50 μm for greyscale images.

Development • Supplementary information

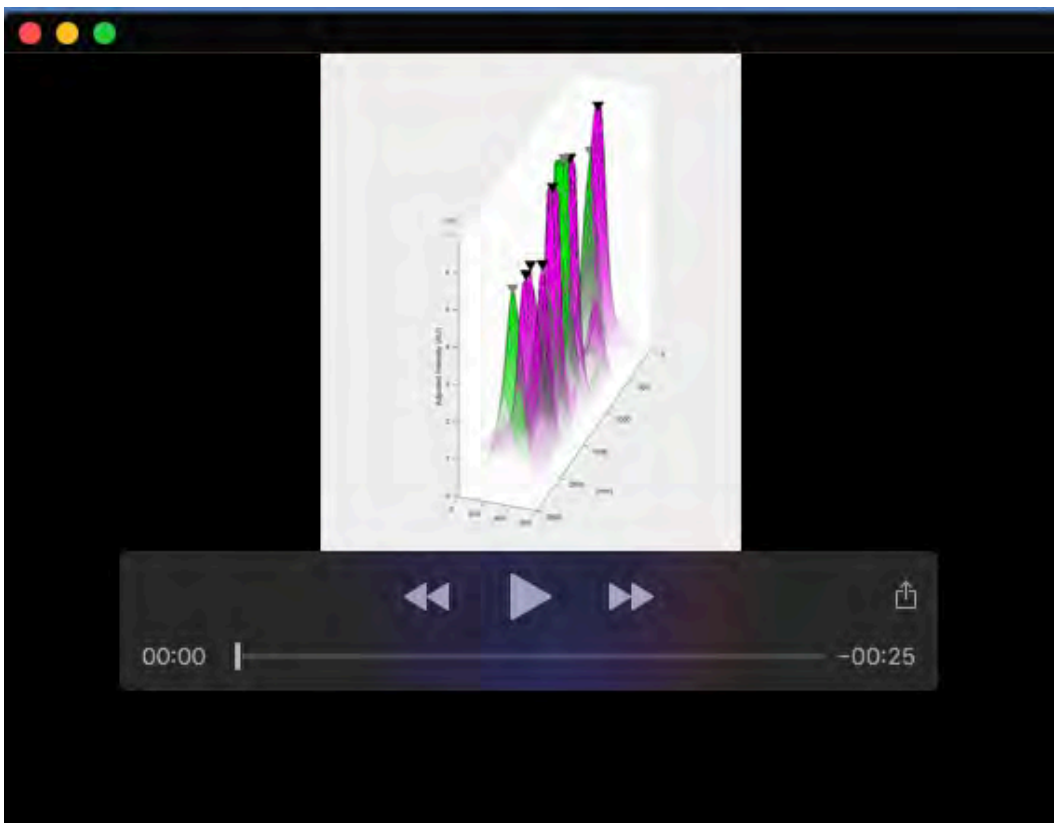

Movie 1. Surface plot of Fz6-3xGFP and tdTomato-Vangl2 peaks in a vertical junction. Rotating surface plot obtained from STED imaging of Fz6-3xGFP and tdTomato-Vangl2 peaks corresponding to the junction in Figure 4C, D. Fluorescence intensity peaks marked by arrowheads.

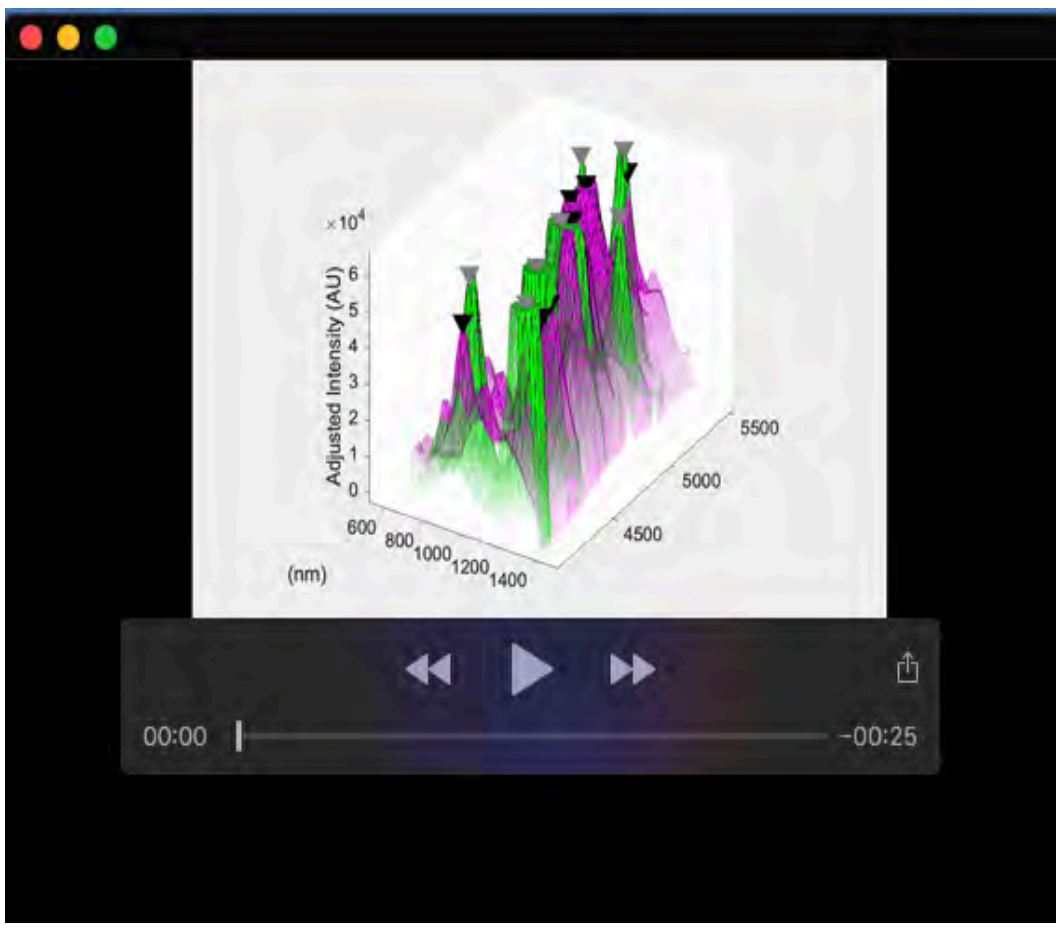

Movie 2. Surface plot of Fz6-3xGFP and tdTomato-Vangl2 peaks in a horizontal junction. Rotating surface plot obtained from STED imaging of Fz6-3xGFP and tdTomato-Vangl2 peaks corresponding to the junction in Figure 4G, H. Fluorescence intensity peaks marked by arrowheads.

Development • Supplementary information

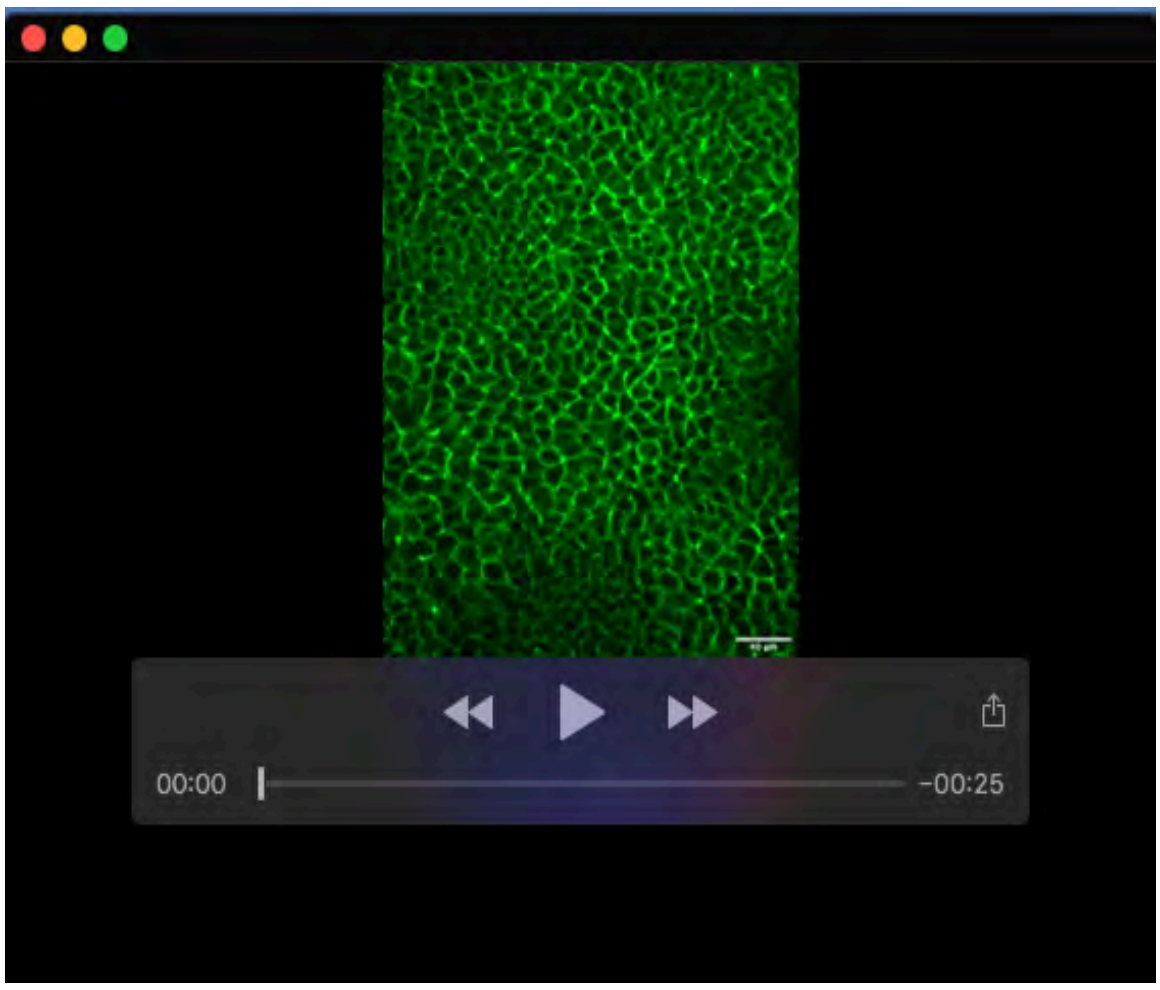

Movie 3. Live imaging of Fz6-3xGFP E15.5 epidermis. Time-lapse imaging of E15.5 Fz6-3xGFP homozygous explants. Imaging was acquired over the course of 7.3 hours with 20 minute intervals. Anterior is to the left. Scale bar, 40 μm.

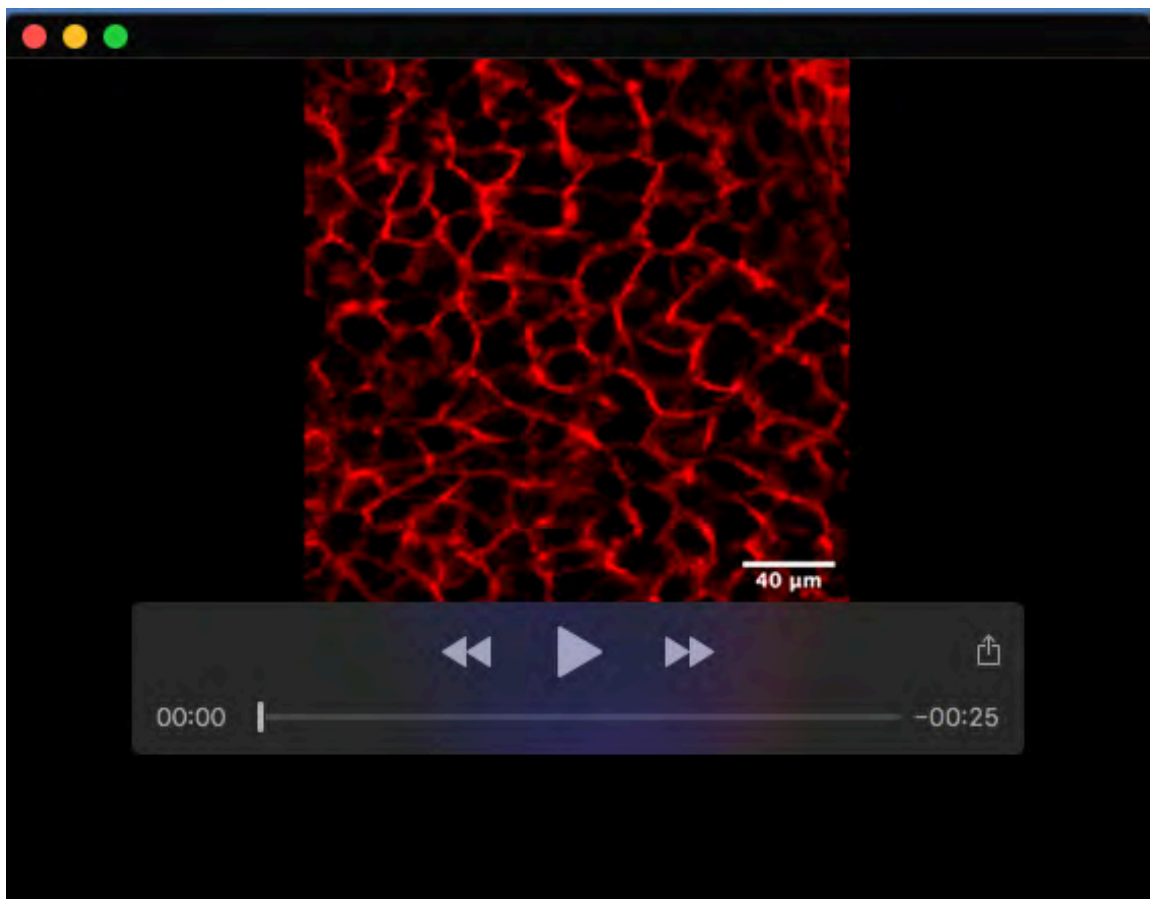

Movie 4. Live imaging of tdTomato-Vangl2 E15.5 epidermis. Time-lapse imaging of E15.5 tdTomato-Vangl2 homozygous explants. Imaging was acquired over the course of 8 hours with 20 minute intervals. Anterior is to the left. Scale bar, 40 μm.

Development • Supplementary information

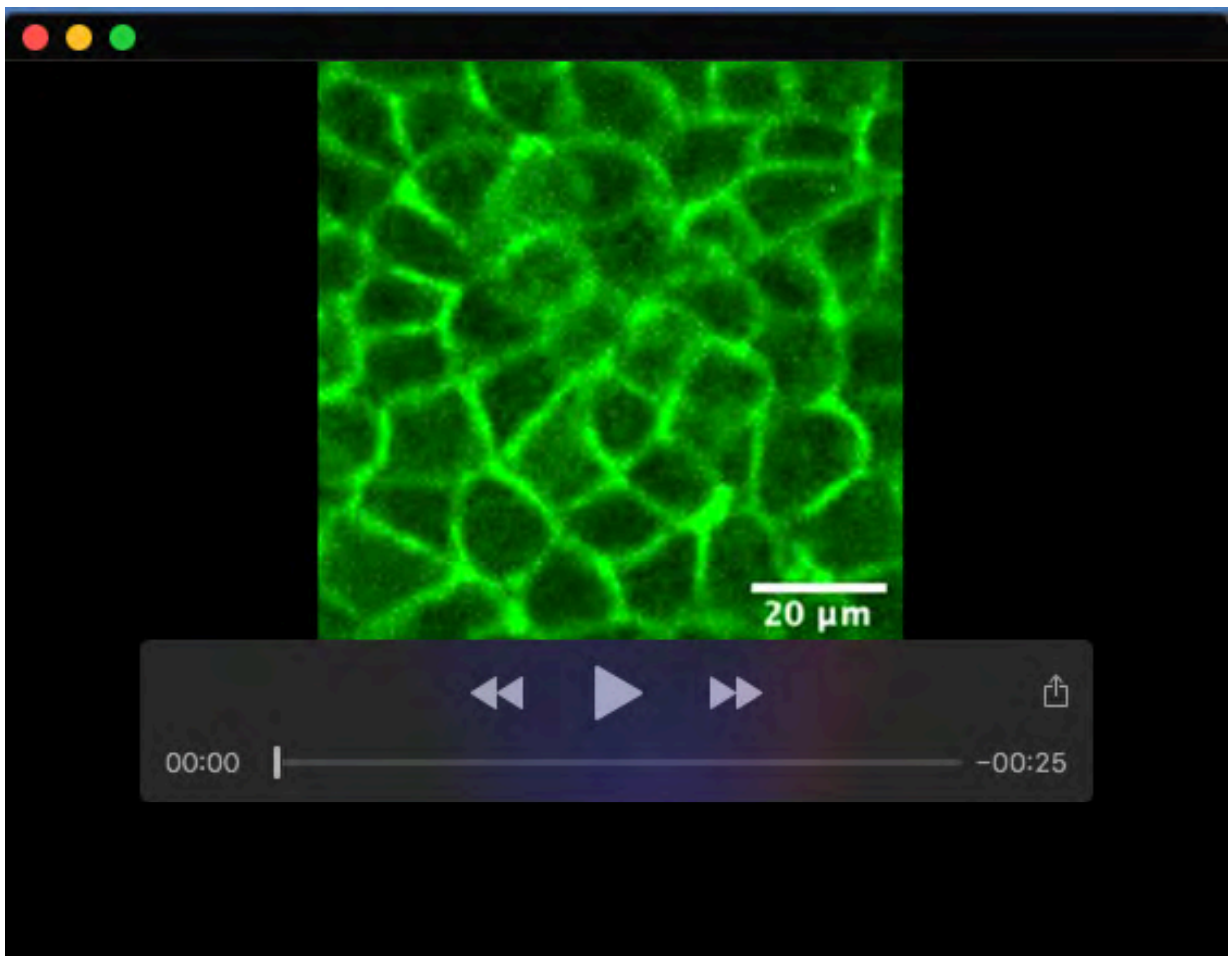

Movie 5. Live imaging of Fz6-3xGFP through cell rearrangements and divisions. Time-lapse imaging of cell rearrangements and divisions in E15.5 Fz6-3xGFP homozygous explants seen in Figure 5B. Imaging was acquired over the course of 7.3 hours with 20 minute intervals. Scale bar, 20 µm.

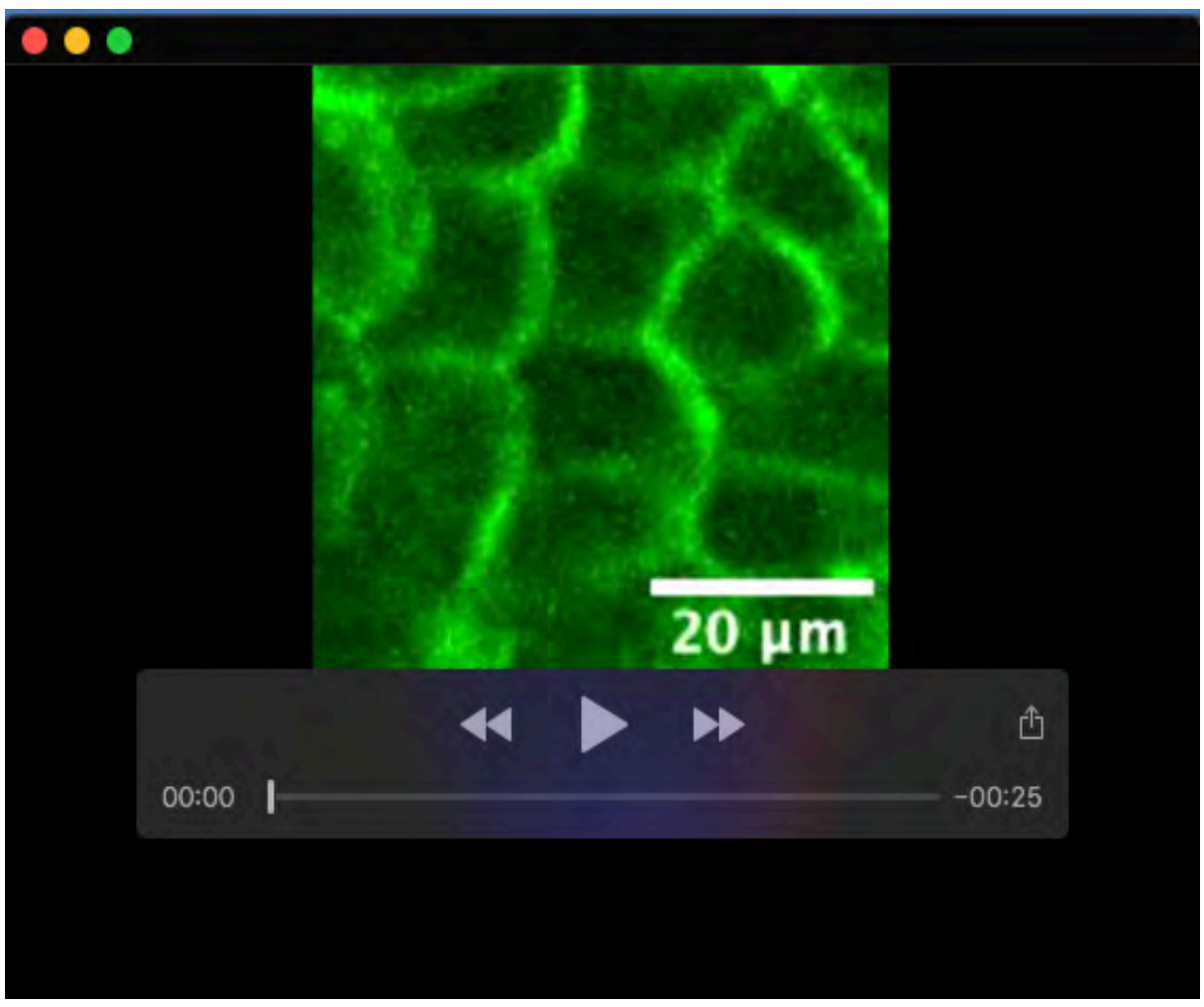

Movie 6. Live imaging of Fz6-3xGFP through cell division. Time-lapse imaging of cell division in E15.5 Fz6-3xGFP homozygous explants seen in Figure 5C. Imaging was acquired over the course of 7.3 hours with 20 minute intervals. Scale bar, 20 µm.

Development • Supplementary information